# Characterizing the Mechanical Properties of a Commercial No-Filler Laser Weld in a 304 Stainless Steel Alloy

A Thesis

Presented in Partial Fulfillment of the Requirements for the

Degree of Master of Science

with a

Major in Mechanical Engineering

in the

College of Graduate Studies

University of Idaho

by

Timothy C. Tilton

Approved by:

Major Professor: Matthew Swenson, Ph.D., P.E.

Committee Members: Michael Maughan, Ph.D., P.E.; Robert Stephens, Ph.D., P.E.

Department Administrator: Gabriel Potirniche, Ph.D., P.E.

May 2023

# Abstract

The mechanical properties of a commercially laser-welded 304 alloy were studied. A sample of the welded material and a sample of the unwelded material were tensile tested to find that the welded sample allowed more ductility while maintaining the same ultimate tensile strength as the unwelded sample. Optical and scanning electron microscopy showed that the weld contained smaller average grain sizes than the surrounding metal. The weld was found by nanoindentation to have a higher hardness than the surrounding metal before the tensile test. Due to the tensile test, the weld experienced lower strain than the surrounding metal, as found by nanoindentation and x-ray diffraction. This information was used to approximate the mechanical properties of the weld and applied to a finite element analysis to corroborate the results with the tensile test data. The approximated strain response of the weld was also compared to a strain hardening model.

# Acknowledgments

I would like to acknowledge the following groups and people for their contributions that were essential to this study.

MacKay Manufacturing, Inc. for performing their laser welding process on the samples.

Dr. Thomas Williams for performing the x-ray diffraction analyses on the samples and providing insight into the technology.

Laurie Delenin for her great work that served as the foundation for this study.

Dr. Michael Maughan and Dr. Robert Stephens for serving on my committee and reviewing my thesis.

And finally, Dr. Matthew Swenson for offering me this opportunity. Your wonderful advice and mentoring I will carry with me through my future endeavors.

## Dedication

This work is dedicated first and foremost to my parents, Chuck and Sue, for all of their love and support they have given me through the years. Without them, I could never have accomplished what I have. I would also like to thank my friends who have supported me while I have worked to complete this thesis, especially my fellow grad student mentors. You have made my final year at the University of Idaho better than I could have hoped for.

# Table of Contents

# List of Tables

# List of Figures

# Statement of Contribution

The following outlines the work done by Laurie Delenin that laid the foundation for this thesis.

**Chapter 2.1 Material and welding procedure**

The welding of the samples was done for Laurie's work. The majority of this section was written by Laurie, with metric conversions done by me. Figure 2.1 is an image taken by Laurie at MacKay Manufacturing Inc. in Spokane, WA, Figure 2.2 was created by Laurie and converted to metric dimensions by me, and Figure 2.3 was also created by Laurie.

**Chapter 2.2 Tensile testing**

Laurie performed the tensile testing of the samples. Laurie oversaw and had the samples machined at the machine shop in the Mechanical Engineering department at the University of Idaho. The sections in this chapter pertaining to these operations were written by her, with metric conversion and some clarification added by me. Figure 2.4 was created by Laurie, with metric conversion done by me.

**Chapter 2.3 Nanoindentation (pre-tensile test)**

Laurie performed the nanoindentation testing on the samples pre-tensile test. The majority of this section was written by her, with some clarification added by me.

**Chapter 2.4 Microscopy (Optical and SEM)**

The optical and scanning electron microscopy and subsequent grain size analyses were performed by Laurie. The majority of this section was written by her, with some clarification on equipment used added by me.

**Chapter 4.1 Tensile testing**

The first half of the tensile test results section was written by Laurie. The literature review was done by me. Figure 4.1 and Table 4.1 were created by Laurie.

**Chapter 4.2 Nanoindentation**

The nanoindentation on the sample pre-tensile test was performed by Laurie. The results in this section were written by her. Figure 4.3 was created by Laurie. The literature review and the results of the nanoindentation on the tensile tested sample were written by me.

**Chapter 4.3 Microscopy**

This section was written by Laurie. She performed both the optical and scanning electron microscopy and the grain size analyses. Figures 4.6 and 4.7 were created by Laurie. Table 4.3 was created by me.

**Chapter 5.2.2 Correlation with mechanical properties**

Laurie performed the Hall-Petch relationship analysis of the grain sizes. The literature review pertaining to this analysis was performed by me.

# Chapter 1: Introduction

Stainless steels (SS) are iron-based alloys with high chromium (18-20 wt %) and nickel (8-10.5 wt %) content [1]. Originally, they were intended for use in cutlery and cookware. Today, they are commonly used in sheet metal form to produce tanks, pipes, and structural members, as well as tools and hard machine components. 304 stainless steel alloys, also known as A2 and 18/8, are some of the most common stainless steels. They are a part of a group known as austenitic stainless steels. These alloys are commonly chosen for their corrosion resistance in mildly corrosive environments. They are also used for food handling and processing due to the effectiveness of sanitization processes.

The tensile behaviors of austenitic stainless steels have been studied a considerable amount. These alloys are known to be quite ductile, elongating at least 50%. The yield strength of 304 SS is 290 MPa in annealed sheet form at room temperature [1]. They are also quite stiff, having an elastic modulus of 193 GPa [1]. The ultimate tensile strength varies widely from study to study, but is at least 500 MPa, commonly can reach 750 MPa, and sometimes even 1050 MPa [1–8]. The plastic deformation behaviors of these steels are highly complex and rely on many factors. Stainless steels have shown a multi-stage strain-hardening behavior in the plastic regime in some situations [3, 5, 6, 9]. This is a characteristic that happens after the material has yielded: just after yield the strain response weakens, it then exhibits an inflection point and the material generates much more resistance to stretching until it reaches its ultimate tensile strength. De and Speer explain that the initial decrease in the slope of the stress-strain curve, or the strain-hardening rate, is due to the formation of ε-martensite and the subsequent increase in strain-hardening rate is primarily due to the formation of α'-martensite [3]. This behavior appears more commonly at room temperature and below [3, 5, 6]. Celada-Cesaro et al. state that ε-martensite formation is favored at these low temperatures [5]. It is also stated that the ε-martensite volume fraction is decreased at higher strains, as the ε-martensite serves as nucleation sites for α'-martensite formation. The stacking fault energy (SFE) has been used to predict the formation of ε-martensite, with lower SFE leading to a higher volume fraction of ε-martensite [5, 10, 11]. As SFE is increased the formation of ε-martensite is suppressed while twinning and slip take its place [10]. Shen et al. state that materials that have an SFE between 18-45 $mJ/m^2$ will show predominantly twinning, while martensitic transformation is more common below 18 $mJ/m^2$, and above 45 $mJ/m^2$ glide dislocations are produced [11].

Applied strain rate is also a major influence on this phenomenon in the strain hardening rate. According to Chen et al., there are two major deformation sequences in austenitic steels dependent on the applied strain [8]. Under high strain rates ($10^4$-$10^5$ $s^{-1}$) the dominant mechanism is the base γ-austenite evolving to twins. Under lower strain rates (10-$10^{-3}$ $s^{-1}$) dislocations and γ-austenite directly

transforming to α'-martensite are the dominant deformation mechanisms. Deng et al. also found that increasing strain rate decreased the volume fraction of α'-martensite in tensile tested 304 [4].

The weldability of 304 is generally considered to be good, although more difficult than most carbon steels [12]. The difficulty of welding 304 comes from overcoming three hurdles. The first being warping, the second is sensitization of the heat affected zone (HAZ) of the weld, and the third being hot cracking of the weld metal. A 50% higher coefficient of thermal expansion than carbon steel presents a greater potential for warping during and after welding [12, 13]. Despite that, a lower thermal conductivity rate allows for a lower heat input due to less heat being drawn away from the weld during the welding. Sensitization is the precipitation of carbides along grain boundaries at elevated temperatures such as during welding. Sensitization can be reduced by reducing the carbon content of the base and filler materials and lowering the temperature and amount of time the metal spends at elevated temperature. Hot cracking is caused by low temperature melting compounds such as phosphorous and sulfur penetrating grain boundaries. As the metal cools, the differential of thermal contraction coefficients between these materials causes cracks to form. Hot cracking can be reduced by lowering the content of these compounds in the base and filler materials [12]. Eliminating the need for filler material, as some laser welding does, reduces the chances of these defects occurring simply by removing a source of them.

Welding stainless steels can affect the microstructure of the material. Normal annealed 304 is purely austenitic. When the metal is subjected to elevated temperature it transforms into δ-Fe, or ferritic steel, and as it cools it transforms back into γ-austenite. However, the cooling rate after welding can change the amount of δ-Fe content and the grain size produced. Rapid cooling rates can cause an incomplete transformation of ferritic δ-Fe to γ-austenite and larger grain sizes [14–16]. According to Kumar et al., lower heat energy input leads to faster cooling times and more δ-Fe content, as well as smaller γ-austenite grain structures due to less time for them to mature; while the opposite is true for higher heat energy input [16].

This change in grain size has the effect of altering the strength of the material in accordance to the Hall-Petch relation as described by Was [17]. Smaller grains correlate to a higher hardness value and a higher yield strength. Welding filler material is often chosen to have a higher yield strength than the base metal in order to produce a joint that is stronger than the base metal in properly executed welds. This can cause an increase in brittle behavior in and around the joint. To combat this, it is common to use a post-weld heat treatment to anneal the weldment or to mechanically introduce compressive residual stresses. Many studies on laser welding of stainless steels have found the fusion zone of the weld to have an equal or lower hardness than the surrounding metal [15, 18–22].

According to Mao et al., the biggest factor in the change in yield strength is the change in grain size [23]. The other contributors are solid solution, dislocation, and precipitation strengthening.

Laser welding has been increasing in prominence due to the ease of integration in roboticized manufacturing. The laser doing the welding is typically computer controlled. Because of this, precise control of the laser parameters such as peak power, pulse parameters, and ramp up and down can all be adjusted to produce high-quality welds. This level of control over weld parameters allows the production of tight tolerance thin sheet metal weldments by avoiding warpage. The laser beam can also offer a deep and narrow fusion zone resulting in lower distortion compared to conventional welding [13]. A smaller mass of metal receives heat input which requires less overall heat input. For these reasons laser welding can produce a more precise and consistent weld product than conventional processes such as gas metal arc welding (GMAW).

The objective of this study is to evaluate and understand the mechanical properties of a specific 304 alloy joined with a commercial laser welding technique. In this work we aim to create a process to approximate the mechanical properties of welded metal using relatively simple and common methods. We approximate the mechanical properties of the weld joint in a laser welded sample of 304 alloy using optical and scanning electron microscopy, nanoindentation hardness data, x-ray diffraction (XRD) analysis, and strain hardening exponent modeling, and finally corroborate those results using a finite element analysis (FEA) model and compare them to a strain hardening exponent model. We also attempt to explain how the weld effected the base material to produce a weldment that both maintains the same ultimate tensile strength and offers more ductility than the base metal alone.

This study began in the spring of 2021 under Dr. Swenson with Laurie Delenin, a J1 visiting scholar from Belgium. She performed much of the initial testing of the samples. The laser welding of the 304 stainless steel samples at MacKay Manufacturing in Spokane, WA. The machining of the samples into testing coupons was done in the University of Idaho's Mechanical Engineering machine shop. Laurie performed the tensile testing at the University of Idaho. She also performed the nanoindentation on the pre-tensile test sample to find the hardness profile across the weld and base metal. The microscopy, both the optical and the scanning electron, were done by Laurie, to find the grain sizes in the weld and the bulk material. She also performed the Hall-Petch relation analysis to correlate the grain size results with the nanoindentation results.

My work on this study began in the summer of 2021, after Laurie completed her time at the University of Idaho and returned to Belgium. It began with an x-ray diffraction analysis performed on a section of the weld that was not used in the tensile test to determine the microstructure phase of the weld material. Later, XRD was done on the tensile tested samples at a location inside the weld zone

and at a location outside the weld zone to find the level of strain hardening in the weld due to the tensile test relative to the bulk material. I then performed a nanoindentation test on the tensile tested sample, using the same settings and techniques as Laurie's nanoindentation test. The results of these tests were used to approximate the mechanical properties of the weld material. These properties were then applied to an FEA model to validate the approximated properties. An evaluation using a strain hardening exponent modeling technique was also used to further corroborate the results. The combination of these techniques enabled a reasonable isolation of the independent mechanical properties of the weld and the base material from the tensile test results.

# Chapter 2: Prior Work

The proceeding sections detail the testing done by Laurie Delenin under the supervision of Dr. Matthew Swenson. This work was done in the spring of 2021 and includes the welding of the sample, the machining of the samples, the tensile tests, the pre-tensile test nanoindention, and the microscopy.

## 2.1 Material and welding procedure

The base metal used in this study is 304 stainless steel (X5CrNi18-10). The percent weight composition of this specific 304 alloy is listed in Table 2.1. The base metal was cut using a hydraulic shear machine from a large sheet into squares of dimensions 50 by 50 mm. The sheet thickness used was 16 gauge (1.52 mm). A clean edge was then made on a milling machine on each square to perform a butt weld. Indeed, because the laser welding done in this study did not make use of a filler material, the edges were required to be straight and smooth enough for the two surfaces to meet with minimal gaps. Figure 2.1 shows the welding configuration and Figure 2.2 shows the drawing of the weld geometry.

Table 2.1 Elemental composition of the 304 stainless steel used.

| **Element** | **C** | **Si** | **Mn** | **P** | **S** | **Cr** | **Ni** | **Mo** | **N** |
|---|---|---|---|---|---|---|---|---|---|
| **Wt %** | 0.05 | 0.44 | 1.05 | 0.029 | 0.002 | 18.22 | 8.05 | - | 0.046 |

The laser welding was performed at MacKay Manufacturing Inc., based in Spokane, WA, on a Miyachi Unitek LW150A laser welder. It was conducted using argon shielding gas to prevent the oxidation of the steel at high temperature. The peak power of the laser was 2 kW. Figure 2.3 shows the power outline: the first flash was performed at 85% of the peak power, and the second and third flashes were respectively performed at 100% and 85% of the peak power. The laser weld was performed with a 16 second weld time on each side of the butt joint (3.18 mm/s welding speed) to reach full penetration. Indeed, the maximal penetration of the weld is approximately 0.75 mm, which is half of the thickness of the samples.

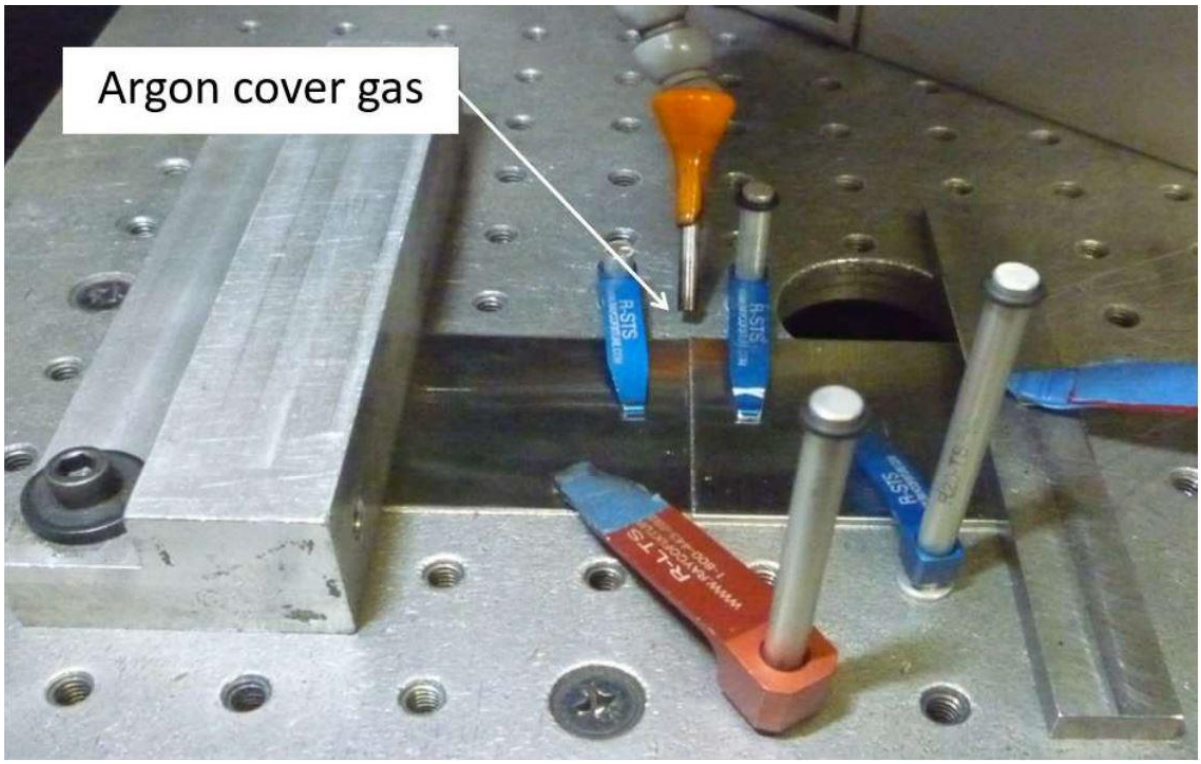


Figure 2.1 A picture of the welding configuration at MacKay Manufacturing Inc.

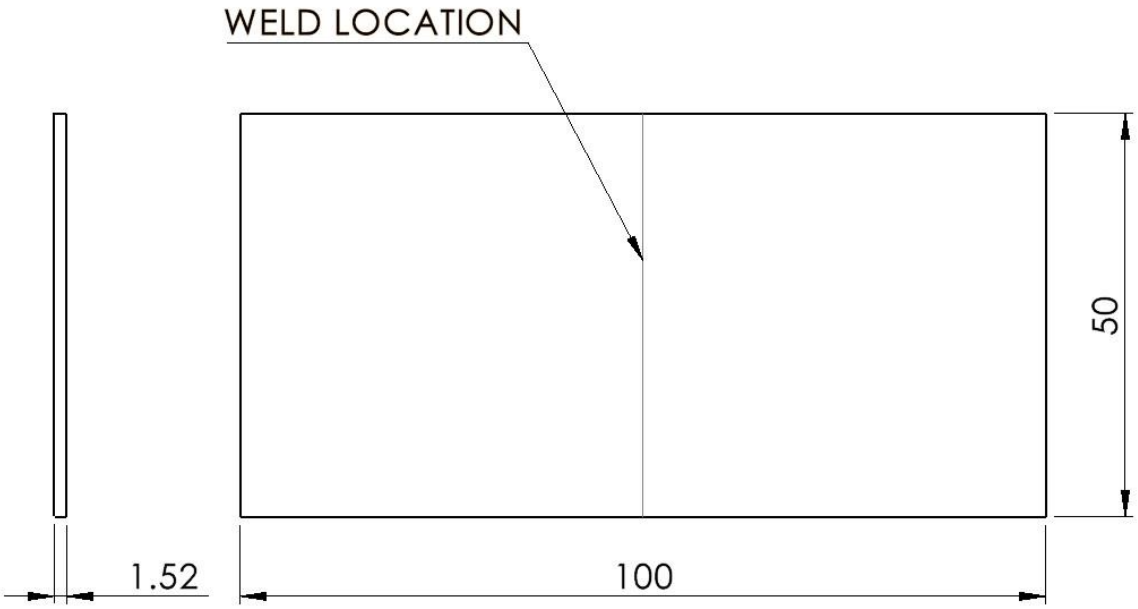


Figure 2.2 Drawing of the sample geometry including the butt weld.

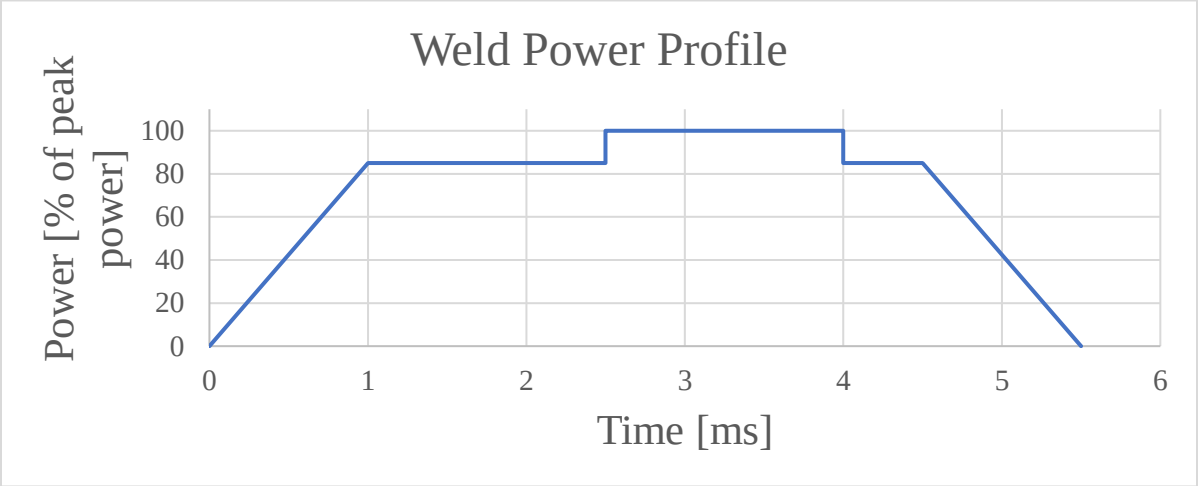


Figure 2.3 Weld power profile over time of weld.

## 2.2 Tensile testing

In order to characterize the mechanical properties and microstructure of the weld, tensile test specimens were cut out from the samples according to the drawing in Figure 2.5. Three rectangular specimens were also extracted from the weldment with dimensions 19.05 by 1.50 mm centered lengthwise on the weld. These were used for scanning electron microscope (SEM) analysis, nano-indentation testing, and x-ray diffraction (XRD) analysis.

The tensile test specimens were extracted from the welded sample using a CNC mill. This shape of tensile test specimens is compatible with the Instron testing machine used at the University of Idaho. The tensile test was performed on a 5982 Instron® Universal Testing System, which has a force capacity of 100 kN, using an extension rate of 25.4 µm/s, and a gauge length of 25.4 mm. The samples were anchored to the machine via pins in the two thru holes. Two specimens of the same shape were also extracted from the bulk material 304 SS.

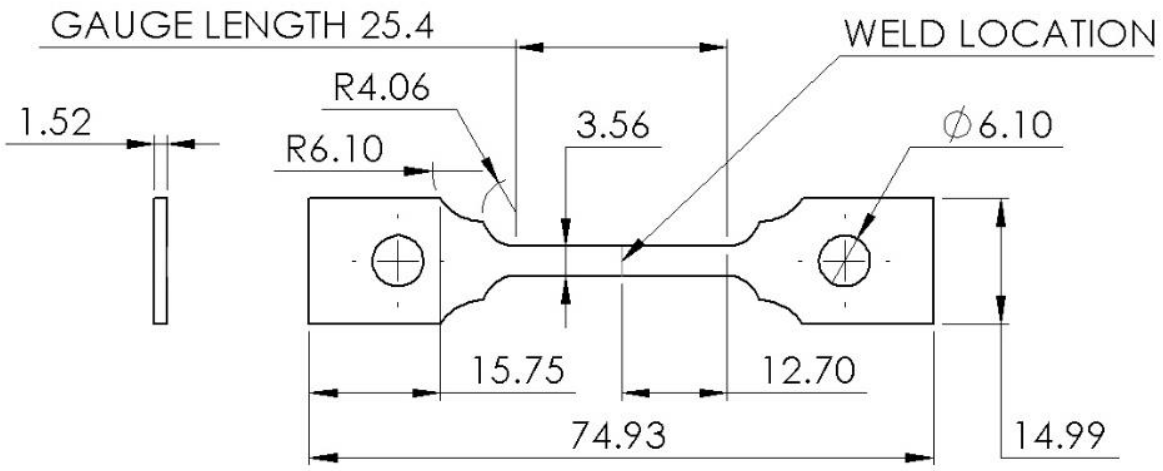


Figure 2.4 Specimen extraction from the welded samples – dimensions in millimeters.

## 2.3 Nanonindentation (pre-tensile test)

The hardness was characterized initially using nanoindentation on the 19.05 by 1.50 mm rectangular specimens. The purpose of this was to observe the difference in hardness between the base material, the weld itself and the heat affected zone. Polishing of the specimen prior to testing was achieved with progressively finer grit sanding disks, from 240-grit to 1200-grit. Quasi-static nano-indentation was then conducted with a KLA-Tencor G200 nano-indenter using a modified constant strain technique. At each indent location, the indenter was set to penetrate in increments of 300 nm to a maximum depth of 3000 nm, retracting to unload 90% of the force on the sample between each depth increment. A total of 120 indents were performed across the surface of the specimen, in two lines of 60 indents, separated by 50 µm (y-axis, along the direction of the weld). The indents were spaced out by 150 µm along each line (x-axis, direction perpendicular to the weld). Figure 2.6 shows a representation of the indentation pattern on the rectangular extraction.

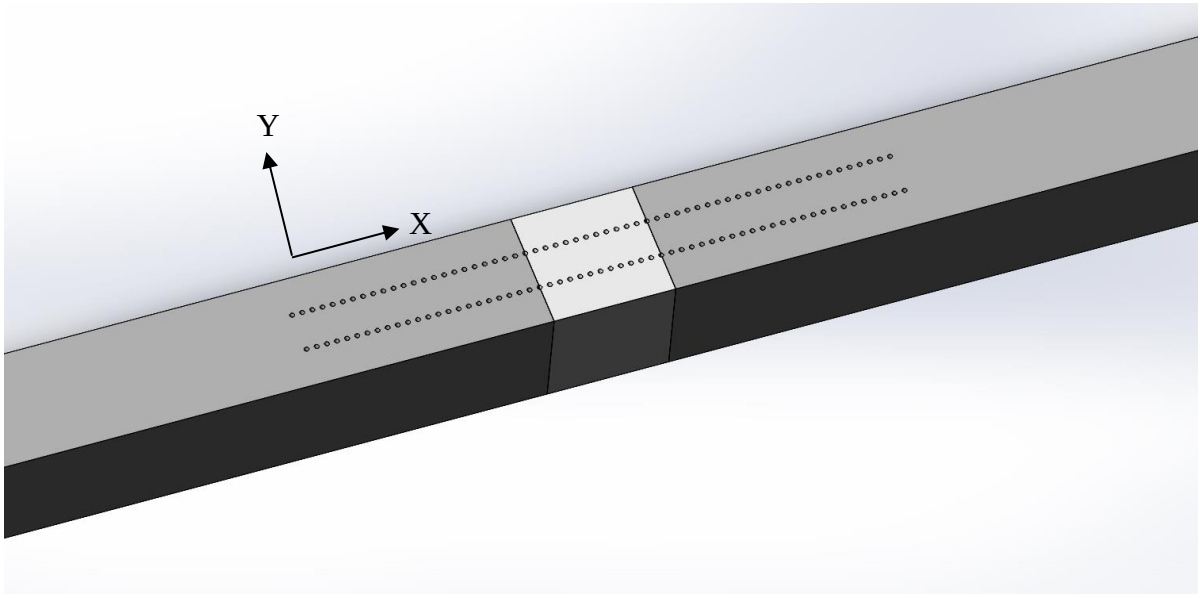


Figure 2.5 A representation of the indent pattern on the rectangular extraction. Note that indent spacing and size are not to scale.

## 2.4 Microscopy (Optical and SEM)

The difference in microstructure between the weld and the base metal was characterized using pictures taken on an Amscope MU2003-BI digital camera mounted on an Amscope ME520TA optical microscope. Images taken using the optical microscope were used to compare grain sizes inside and outside of the weld. This was done using the intercept method. It consists of drawing a few straight lines across an image and counting the amount of intersected grain boundaries. The mean intercept length, $\bar{I}$, can then be determined by

$$\bar{I} = \frac{Total\ length}{Number\ of\ intercepted\ grain\ boundaries} \tag{2.1}$$

and is considered as a measure of the effective grain diameter [15].

In addition to optical microscopy, images were taken using a Tescan Vega 3LMH scanning electron microscope (SEM). The SEM requires proper preparation of the specimen. Polishing was achieved with progressively finer grit sanding disks, from 240-grit to 1200-grit, followed by polishing using 3 µm then 1 µm diamond suspension. The specimen was then electro-chemically etched in order to see the microstructure, using a 10% oxalic acid solution, and a power source maintained at a voltage of 10 V. After the images were taken, grain size was calculated by measuring the length and width of each grain and then finding the effective diameter. This diameter,

$$d_{eff} = \sqrt{Length\ x\ Width} \tag{2.2}$$

corresponds to the diameter of the circle that has the same area as the ellipse with diagonals equal to the length and width of the grain.

# Chapter 3: Methods

The proceeding sections detail the physical testing I performed in this study. This work began in the summer of 2021 and includes the post-tensile test nanoindentation and the x-ray diffraction.

## 3.1 Nanoindentation (post-tensile test)

Nanoindenting was also performed on one tensile-tested sample. The tensile test left the weld intact allowing the indentation test to be completed across the weld. This specimen was also polished with progressively finer grit sandpaper starting from 240-grit to 1200-grit and after that polished with 3 μm and 1 μm diamond suspension compound. As before, this test was done using the KLA-Tencor G200 nano-indenter, except this time in two rows of 90 indents 50 μm apart, spaced by 150 μm along each row. Both rows started in the base metal on one side of the weld and continued across and through the weld into the base metal on the other side. Figure 3.1 shows a not-to-scale representation of the indent pattern on the tensile sample. The indenter was again set to penetrate the material to a maximum depth of 3000 nm in 300 nm depth increments for each indent. All tensile and nanoindentation tests were done at room temperature.

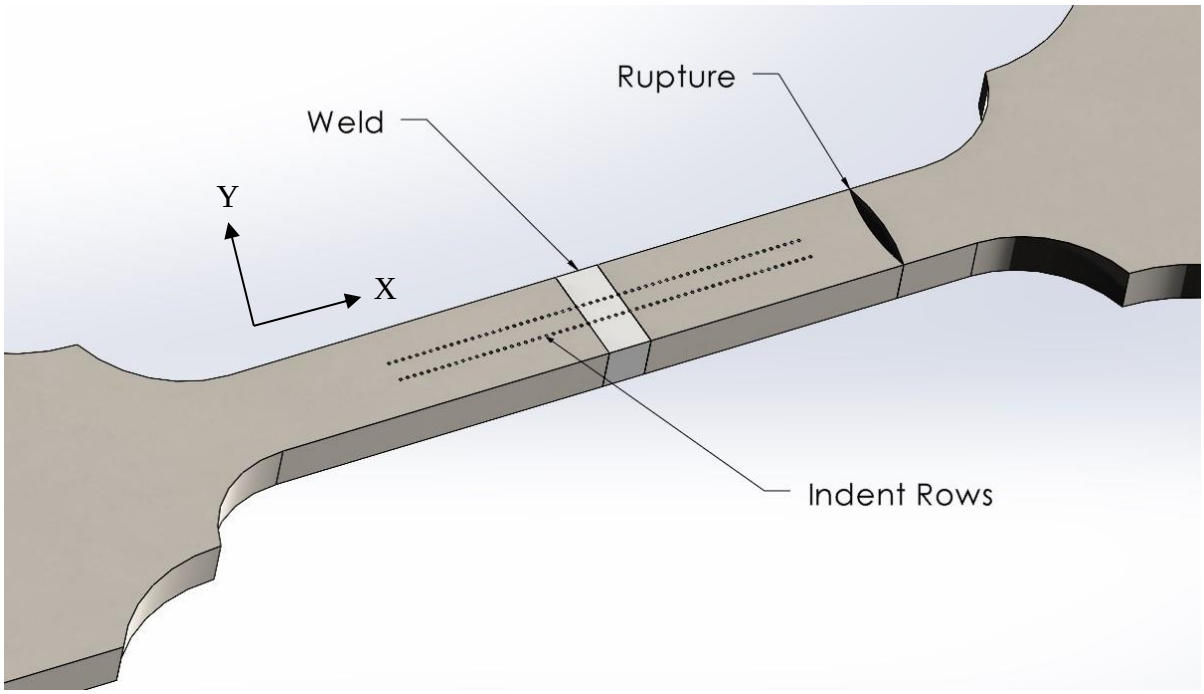


Figure 3.1 A representation of the indent pattern on the tensile-tested specimen 3. Note that indent spacing and size are not to scale.

## 3.2 X-ray diffraction

X-ray diffraction was used to determine the phase of the steel in the welded samples before and after the tensile test was performed on them. Prior to each XRD test the samples were prepared by polishing using progressively finer grit sanding disks, from 240-grit to 1200-grit. The samples were mounted to a glass backing with mounting wax to reduce erroneous background data. The XRD was performed on the material before and after it was tensile tested. Prior to the tensile test the XRD was performed in the cross-section of the weld on one of the rectangular extractions. Post-tensile-test the XRD was performed on the surface of the tensile sample in the weld and the bulk material to compare the strain-induced phase transformation in each. The machine used was a Bruker D8 using Cu Kα radiation, $\lambda = 1.54056$ nm, and a 0.5 mm collimator. This machine has a 2-D 'area' type collector that gathers data from a range of angles during each collection run, or step. Scans were taken in three steps. For the first step the emitter was set to 12 degrees and the collector was set to 25 degrees. For the second step the emitter and collector were both set to 30 degrees, and for the final step they were set to 45 and 35 degrees, respectively. The positions on the last scan were chosen to avoid a collision in the machine. These settings resulted in $2\theta$ ranges of 21.7 – 52.3 degrees, 44.7 – 75.3 degrees, and 64.7 – 95.3 degrees for the three steps respectively. For the pre-tensile-test sample, each of these scan steps collected data for 5 minutes while the scans on the post-tensile-test sample collected data for 20 minutes each.

The data were processed in MATLAB. Each scan step from the machine generated its own data set and the following was performed on each.

1. A first-degree polynomial was fit to the data.
2. The fit line was subtracted from the data to achieve an average of 0.
3. A data point was found at a $2\theta$ value that overlapped and was sufficiently close to a point in the adjacent data set ($\pm$ 0.5° $2\theta$).
4. The data outside of this point relative to the center of the set were truncated

Once this was complete on the three data sets for one XRD run, they were plotted. These steps were taken to reduce the background noise on the graphs. The peaks of the data were difficult to compare between the separate XRD tests beforehand and doing this reduced that difficulty. This process is shown in Appendix A.

# Chapter 4: Results

## 4.1 Tensile testing

Figure 4.1 presents the results of the tensile test. Specimens 1 and 2 are made wholly of the bulk material 304 SS, while specimens 3 and 4 are the laser welded samples. For the two latter specimens, the tensile test ended with rupture outside of the weld zone. This left the welded area intact so the nanoindentation could be performed in the same manner as the non-tensile-tested specimen. Figure 4.2 shows the welded specimen 3 after the tensile test was completed with the rupture outside of the weld zone. Table 4.1 gives the values of different mechanical properties that were extracted from the tensile test results along with the corresponding expected values. Expected values here represent information given by the foundry and from the American Society for Metals [1].

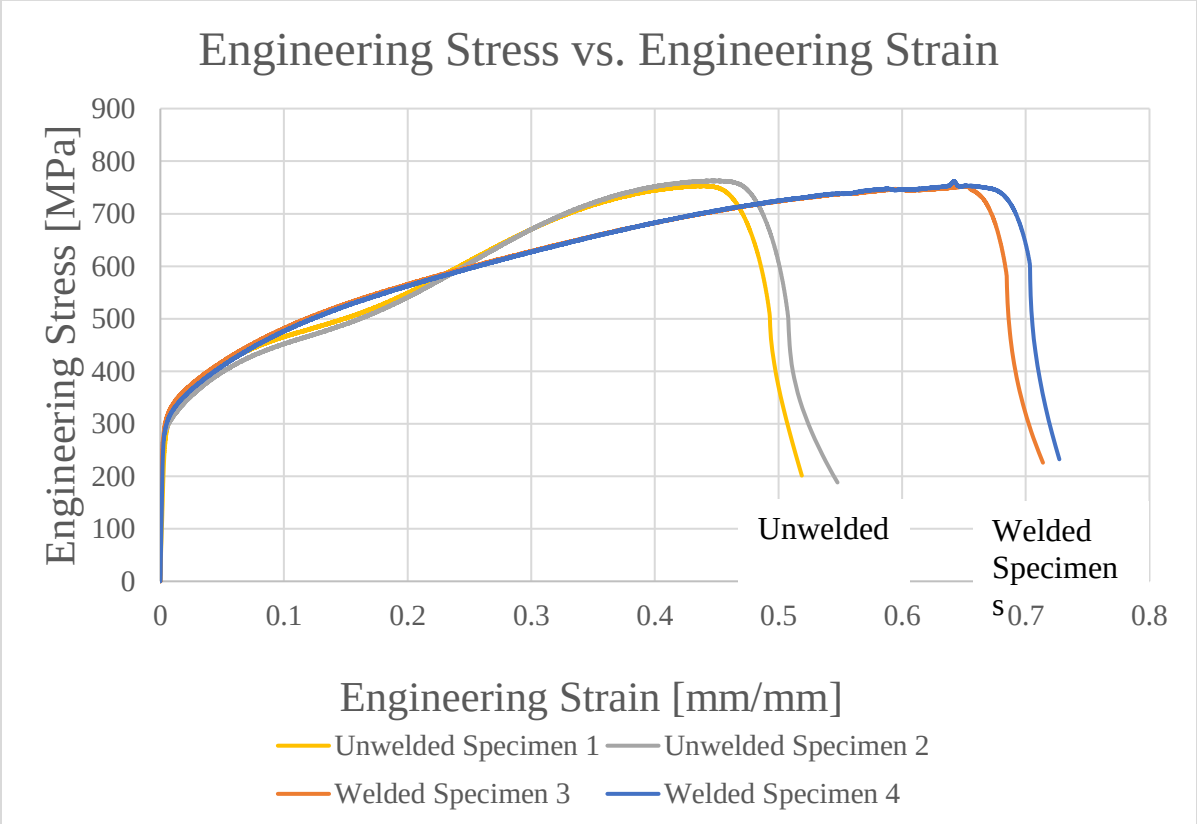


Figure 4.1 Stress vs. strain graph resulting from the tensile testing. Specimens 1 and 2 are the unwelded samples and Specimens 3 and 4 are the welded samples.

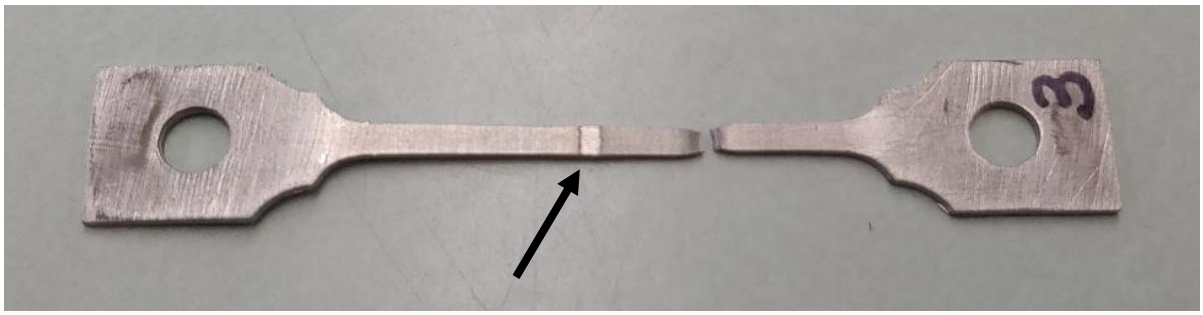


Figure 4.2 Welded specimen 3 after tensile test – rupture outside of weld area. The arrow indicates the weld joint.

Table 4.1 Mechanical properties extracted from the tensile test.

| **Mechanical property** | **Expected** | **Unwelded Specimen 1** | **Unwelded Specimen 2** | **Welded Specimen 3** | **Welded Specimen 4** | **Average (1&2/3&4)** | **Standard Deviation (1&2/3&4)** |
|---|---|---|---|---|---|---|---|
| **Young's Modulus *E* [GPa]** | 193 | 80.7 | 205.1 | 187.6 | 126.4 | 150.0 | 57.2 |
| **Yield strength $\sigma_{0.2\%}$ [MPa]** | 295 | 290.8 | 275.3 | 295.4 | 293.5 | 288.8 | 9.2 |
| **Tensile strength $\sigma_u$ [MPa]** | 668 | 753.7 | 763.5 | 753.3 | 762.1 | 758.2 | 5.4 |
| **Elongation *A* [%]** | 59 | 51.6 | 54.7 | 71.3 | 72.5 | 53.2 / 71.9 | 1.6 / 0.6 |

The trends here are very interesting. All four samples here have close to the same ultimate tensile strength. The ultimate tensile strengths for specimens 1 and 2 are 753.7 and 763.5 MPa respectively. The ultimate tensile strengths for specimens 3 and 4 are very close to the prior two at 753.3 and 762.1 MPa respectively. These results from all of the samples exceed the expected tensile strength of the material as specified by the supplier as shown in Table 4.1. They are also consistent with results of other studies. Others have found ultimate tensile strengths in the range of 700-790 MPa engineering stress at low strain rates (~$10^{-3}$ $s^{-1}$) and at room temperature for 304 alloys [4, 6, 7, 9, 24, 25]. Specimens 1 and 2 are shown to stretch an average of 53.2% while specimens 3 and 4 stretched an average of 71.9%. The latter stretched 1.35 times further than the former.

Another interesting phenomenon occurs. For specimens 1 and 2, the curves in Figure 4.1 show two inflection points towards the beginning of the plastic phase. According to Shen et al. [11], this drop in the curve is due to dislocation slip in the material. Depending on the strain rate used, these dislocations are more or less present. In this study, the same strain rate was used for all the specimens. This means that the presence of the weld has an influence on the dislocation activity. The twinning mechanism will also be impacted, as well as the nucleation of ε-martensite [11]. This inflection behavior has been shown to be present in 304 when tensile tested at temperatures at or below room temperature in other studies. One such study by De and Speer tensile tested 304 at temperatures of -80, -50, -25, 0, 25, 95, 135, and 180° C [3]. This s-curve behavior was present in the samples tested at 0° C and below. As temperature decreased the s-curve became more pronounced and began at lower strain values. In a study by Byun et al. that compared tensile test results of 316LN annealed, 316 annealed, 304 annealed, and 20% cold-worked 316LN steels in temperatures of -150, -100, -50, 20, 100, 200, and 400° C, the annealed 304 showed this behavior at temperatures of -50° C and below [6]. As in the De and Speer study, the s-curve became more pronounced as temperature decreased. In both studies, ultimate tensile strength increased as temperature decreased. The strain rates used in these studies were $5.2 \times 10^{-4}$ $s^{-1}$ for De and Speer, and $10^{-3}$ $s^{-1}$ for Byun et al., compared to an extension rate of 25.4 μm/s ($10^{-3}$ $s^{-1}$ strain rate) for our study. Yet another study showed this behavior in a 304L alloy tensile tested at $1.2 \times 10^{-3}$ $s^{-1}$ [24].

Of note in Table 4.1 is the wide range of values found for the Young's modulus for the four specimens. This could be explained by the single-sided type extensometer used for the tensile test. This type of extensometer is prone to providing gross errors due to slippage or slight misalignments on the specimen. They are generally not used for modulus gathering due to such errors [10]. Taking this into consideration and looking at Figure 4.1, this makes sense. The elastic region where this measurement would be taken is condensed into a very small range of strain values. If the extensometer needs to read strains of more than 70%, then it should follow that it would have difficulty reading strains on the order of 0.1%. Strains this small on a gauge length of 25.4 mm would be 0.025 mm – a very small measurement. This does not invalidate the test, but merely suggests that the resulting modulus of elasticity measurements are unreliable. To deal with this the ASTM E 646 suggests the use of nominal values of the modulus for subsequent calculations [11].

## 4.2 Nanoindentation

Figure 4.3 shows the nano-hardness profile across the weld for two sets of data; each obtained by one row of indents as described in section 2.2. In this graph, hardness, in GPa, is plotted against the distance from the approximate center of the weld for each indent. This hardness is the

average hardness of the final four depths (2100, 2400, 2700, and 3000 nm) at each location. A jump in the hardness occurs between -900 and 900 μm and can be attributed to the weld. From the graph, the weld was determined to have an average hardness of 2.51 GPa. The standard deviation for this region was 0.11 GPa. An overall average hardness was also determined for the bulk material (between −4050 μm and −1800 μm, and between 1950 μm and 4800 μm): 2.10 GPa. The standard deviation for this region was 0.10 GPa. These average values are lower than other published results using Berkovich indenter tips. Weaver et al. found a hardness value of 3.04 ± 0.14 GPa in a 304 alloy with indenter tip radii of 1 and 10 μm (depth of about 230 nm) [28]. Natali et al. found a hardness value of about 4 GPa in a 304 alloy at indent depths of 700 – 1700 nm [29]. Luo et al. found hardness values ranging from 2.38 to 3.50 GPa at indenter loads of 500 – 2000 μN [30]. Lu et al. tested coarse-grained and nano-grained 304 alloys and found hardness values of 2.25 and 7.4 GPa respectively at sample loads of 3000 mN [31]. These studies as well as our data showed that hardness values decreased with increasing indent depth. Studies by Kumar et al. and Cui et al. both found that the hardness in the respective laser welds in stainless steels were harder than the surrounding material, similar to our results [16, 32]. These are in contrast to many other studies that found the reverse [15, 18–22]. Also of note is that the HAZ is sometimes found, as was the case with a study by Kong et al., to be harder than both the fusion zone of the weld and the base metal, which is in contrast to our results [22].

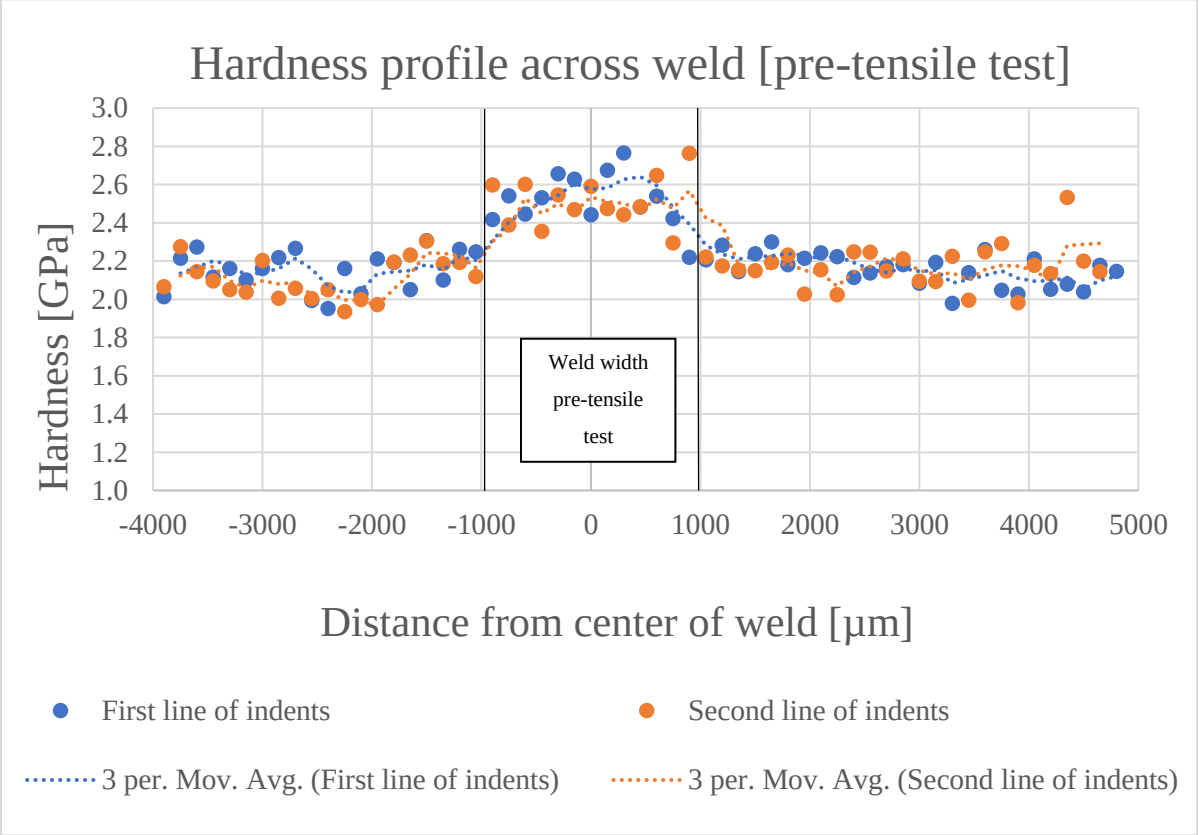


Figure 4.3 Nanoindentation hardness profile across the weld prior to tensile testing.

The hardness data from the nanoindenting on the tensile-tested sample showed the opposite trend of the pre-tensile test nanoindentation. Figure 4.4 shows the hardness profile from the nanoindentation test on the tensile-tested specimen 3. In this graph the positive distances from the center of the weld (right side) of the post-tensile test data advance towards the location of the rupture from the tensile test. This shows that the overall hardness of both the bulk and the weld increased from the tensile test. The weld had a lower hardness than the bulk material surrounding it after the tensile test. The weld was determined to be between -1200 and +1200 µm from the center of the weld. Taking the average from the four final depths (2100, 2400, 2700, and 3000 nm) at these locations, the average hardness of the weld was found to be 5.01 GPa with a standard deviation of 0.29 GPa. Taking the average of the four final depths at the remaining locations the average hardness of the bulk was found to be 5.26 GPa, with a standard deviation of 0.37 GPa. The standard deviations from these data are much higher than those of the pre-tensile test. The averages and standard deviations for both hardness profiles are shown in Table 4.2.

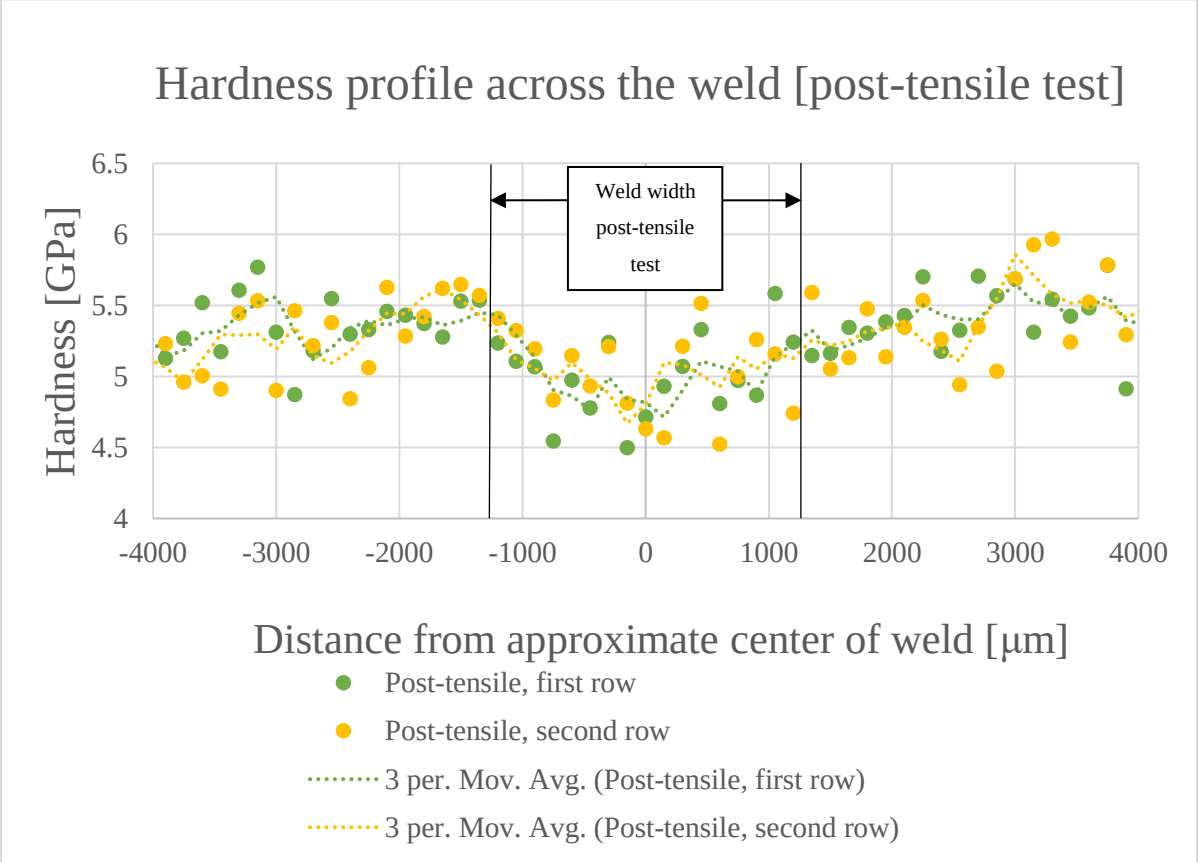


Figure 4.4 Nanoindentation hardness profile across the weld after tensile testing.

Table 4.2 The averages and standard deviations of the hardness of the 304 SS obtained from nanoindentation before and after tensile testing.

| | **Hardness before tensile test** | | **Hardness after tensile test** | | **Increase in average hardness due to tensile test [GPa]** |
|---|---|---|---|---|---|
| | **Average [GPa]** | **Standard deviation [GPa]** | **Average [GPa]** | **Standard deviation [GPa]** | |
| **Bulk** | 2.10 | 0.10 | 5.26 | 0.37 | 3.16 |
| **Weld** | 2.51 | 0.11 | 5.01 | 0.29 | 2.50 |

Figure 4.5 shows an image of the cross section of the weld. This image was taken with an Amscope MU2003-BI microscope digital camera under 5X magnification. In this image, one surface of the sample is at the top of the image while the other surface is at the bottom. The two weld beads are visible from the laser weld performed on each side of the 304 plates. The darker area in these beads would be the actual weld zone while the area just outside of that would be the heat affected

zone, and the rest of the image would be the bulk material. It can be seen that the HAZ narrows as it gets closer to the surface of the sample. This could explain why the HAZ is not represented in the hardness profiles of the two samples.

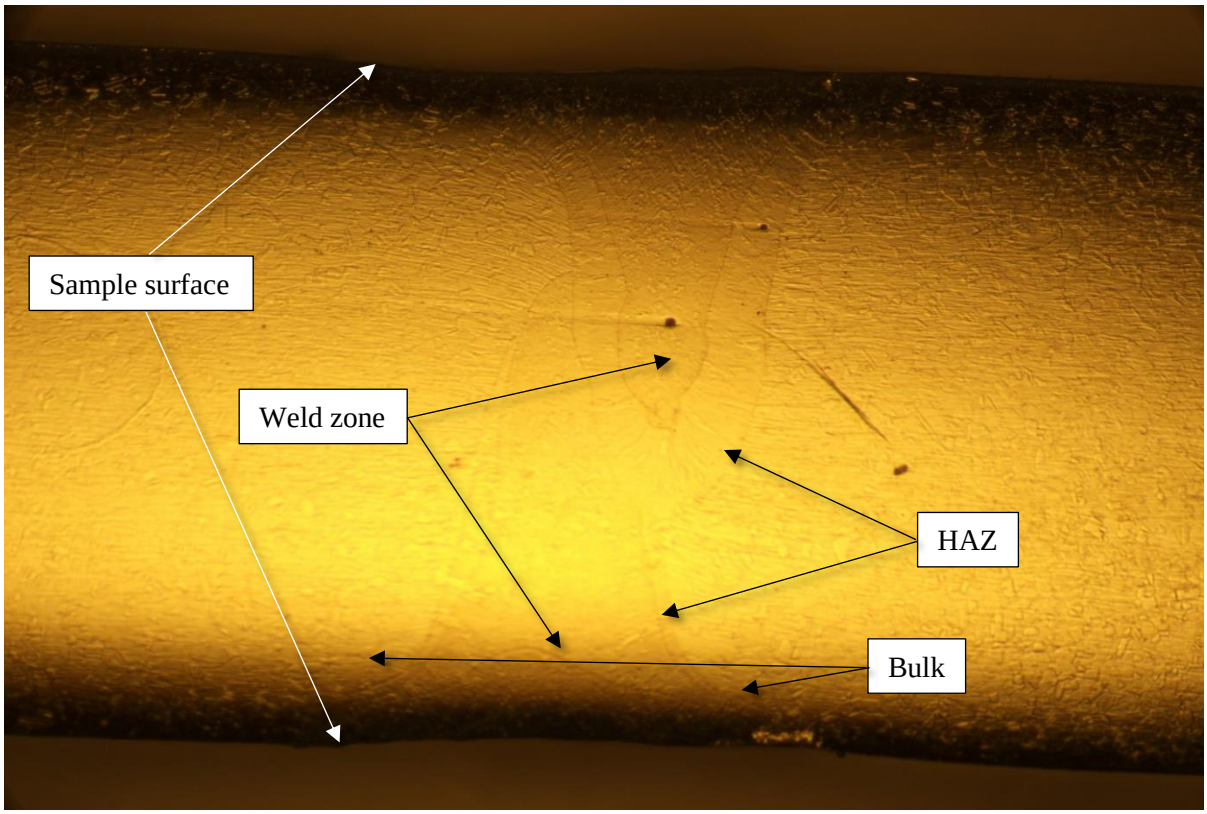


Figure 4.5 An image of the cross section of the laser weld in the 304 alloy.

## 4.3 Microscopy

The SEM analysis and optical microscopy provided images of the microstructure in different regions of the samples. Two different techniques were then used to determine the size of the grains. Table 4.3 gives the results for the grain size inside and outside of the weld, using both methods.

On images obtained by optical microscopy, the intercept method of finding the average grain size was used. Figure 4.5 shows the analysis performed inside and outside the weld zone. The resulting mean intercept length outside of the weld zone was computed to be equal to $\bar{I} = \frac{2458.73}{185} =$ 13.29 µm. The resulting mean intercept length inside the weld zone was computed to be $\bar{I} = \frac{1904.13}{273} =$ 6.97 µm.

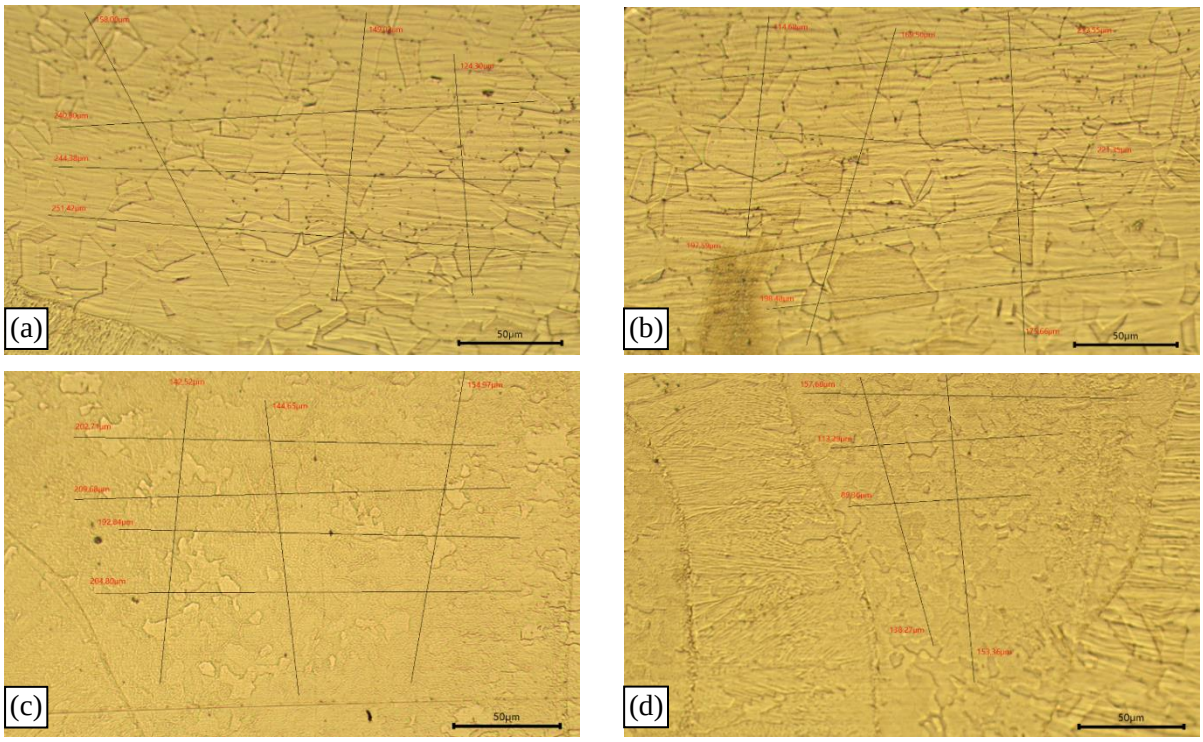


Figure 4.6 Mean intercept length grain size computation method done on the pre-tensile test samples. The top two images (a) and (b) were taken outside the weld zone. The bottom two images (c) and (d) were taken inside the weld zone.

The SEM analysis resulted in higher magnification images. These images were then used for the method of finding the effective grain diameter. Figure 4.6 shows the analysis performed on an image collected from inside and outside the weld. The resulting mean effective diameter was computed equal to $d_{eff}$ = 6.68 µm inside the weld. The mean effective diameter outside the weld was found to be 14.10 µm. The resulting grain sizes found with the optical microscopy and the SEM methods inside and outside the weld are shown in Table 4.3.

Table 4.3 Intercept lengths and effective diameters of grains as measured in and out of the weld.

| | Optical Microscopy | SEM | |
|---|---|---|---|
| | **Mean intercept length [µm]** | **Effective diameter [µm]** | **Standard Deviation [µm]** |
| **Outside the weld** | 13.29 | 14.10 | 6.16 |
| **Inside the weld** | 6.97 | 6.68 | 1.96 |

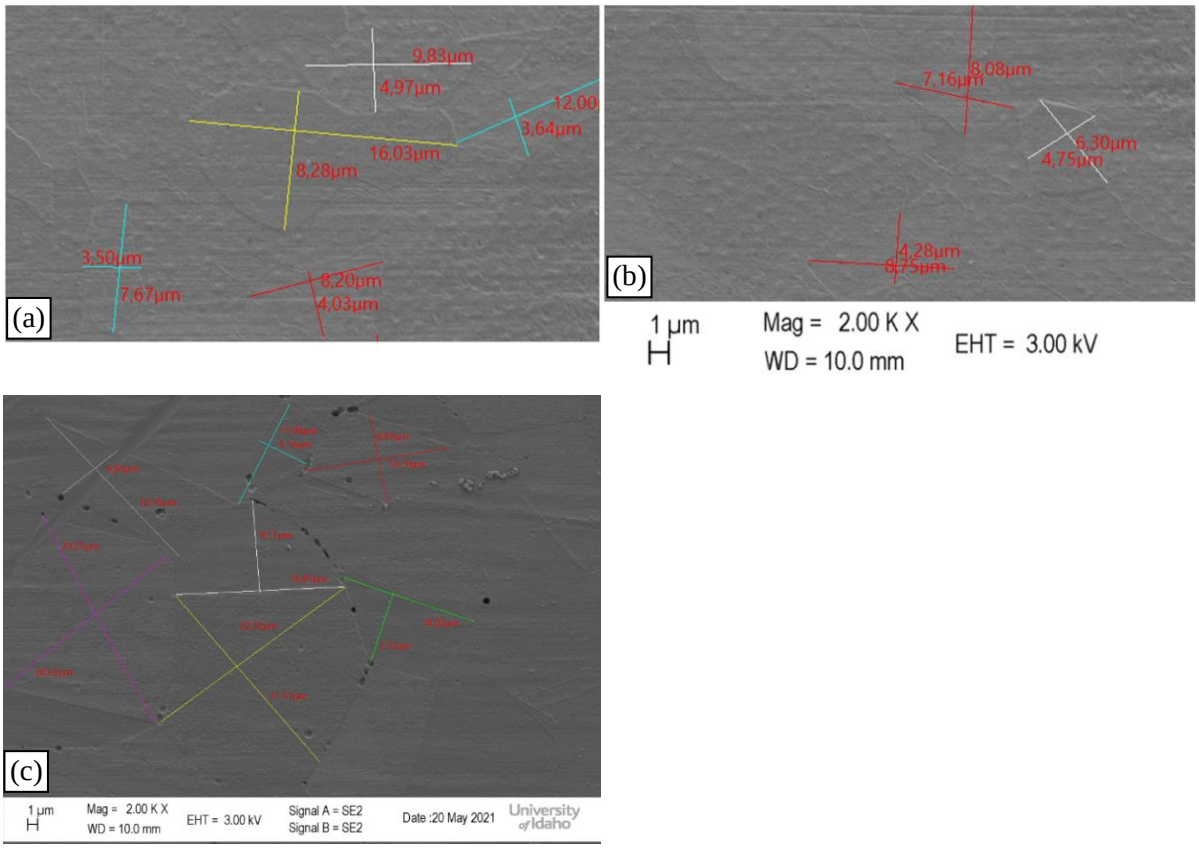


Figure 4.7 Equivalent ellipse grain size computation method. Images (a) and (b) were taken inside weld zone. Image (c) was taken outside of the weld zone.

## 4.4 X-Ray Diffraction

The XRD results for the weld material in the pre-tensile-test specimen are shown in Figure 4.7. Four peaks are shown at 43.7, 50.8, 74.7, and 90.7 degrees 2$\theta$. There are no other perceptible peaks in the data. These peak locations are consistent with pure austenitic stainless steel. This correlates well to the findings of Chen et. al.[8]. However, a study by Yan et al. found different results [14]. In the study, XRD data of welded joints in 304 stainless steel done with tungsten inert gas (TIG), laser, and a hybrid of the two were compared. Their XRD showed that both δ-Fe and γ-

austenite were present in all three joints. In both the TIG and hybrid joints the XRD showed a higher content of austenite than ferrite, while the opposite was true of the laser joint.

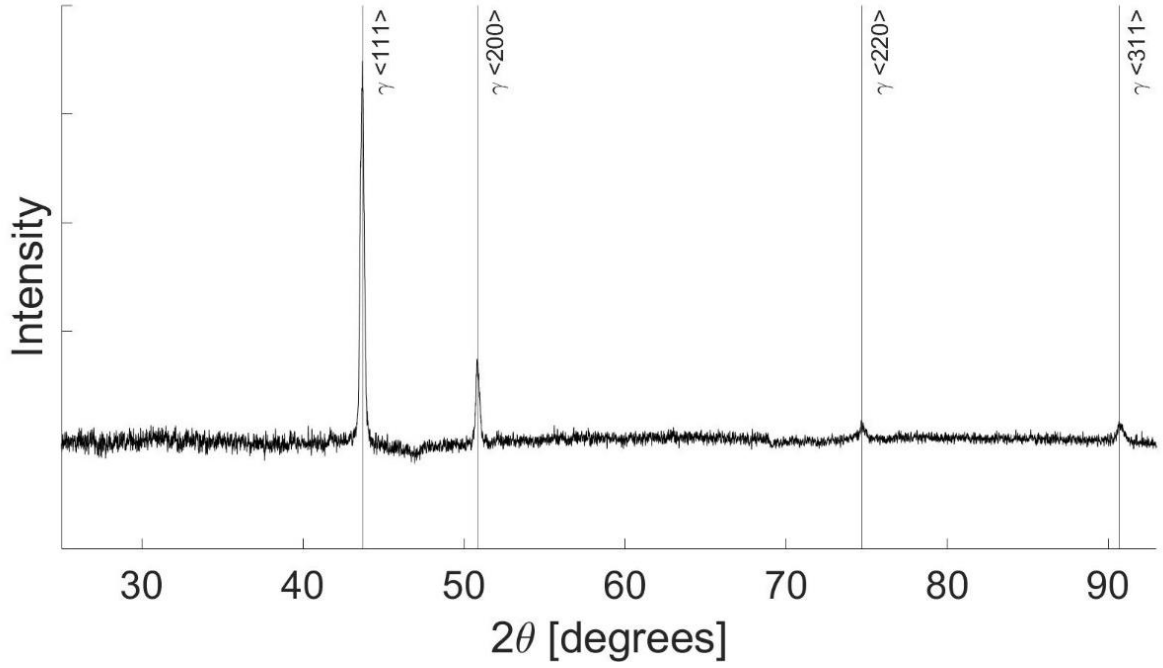


Figure 4.8 X-ray diffraction data in the weld of the pre-tensile-test sample.

The results of the XRD on the tensile tested samples are shown in Figure 4.9. The results show the reflected spectra when the x-ray was directed at the weld material and the bulk material. The location that the x-ray was directed towards was approximately 1 cm away from the weld. This was chosen to be sufficiently away from the weld to not be influenced by the heat affected zone of the weld. The same γ-austenite peaks from the pre-tensile-test material can be seen in both the bulk and weld post-tensile-test, though at significantly reduced amounts. Peaks at 44.6, 64.8, and 82.0 can also be seen in both materials. These peaks correspond to α'-martensite, although both δ-Fe and α'-martensite can be represented at an angle of around 44 degrees. Knowing that there was no δ-Fe present prior to tensile testing and no other peaks for δ-Fe are shown, we can conclude that it is not present in the tensile-tested samples and the peak at 44.6 degrees is in fact α'-martensite. The peak at 44.6 degrees shows that much less α'-martensite formed in the weld material than in the bulk material. Based on the peak values the ratio of α'-martensite to γ-Fe is 2.4 in the bulk material and 1.7 in the weld material.

It can be noted that no ε-martensite was detected in any of the XRD scans. Choi and Jin and Fujita and Katayama also experienced γ-austenite transforming to α'-martensite after straining of a 304 stainless steel with no ε-martensite forming [10, 33]. They explain that the sequence of

deformation modes they had was γ-austenite → mechanical twins (γ') → α'-martensite transformation [33]. A study by Chen et al. investigated the phase transformation in a 304-type stainless steel due to induced strain via surface mechanical attrition treatment (SMAT). They also discovered the transformation from austenite to martensite after straining, with the transformation rate increasing with increasing strain rate [8]. Using more conventional strain application by tensile testing 304-type stainless steels Shen et al., and Deng et al., found similar results [4, 11]. These studies are in contrast to studies by De and Speer [3], Celada-Casero et al. [5], and Soares et al. [9]. Both of these studies showed a presence of ε-martensite after strain was applied to a 304, albeit in small amounts relative to other phases. De and Speer showed it was present after the 304 was subjected to 15% true strain. The Celada-Casero et al. and Soares et al. studies showed that ε-martensite was present maximally at engineering strains between 20% and 30%. In all the studies that performed XRD at advancing strain increments, they all showed α'-martensite to increase and γ-austenite to decrease with increasing applied strain.

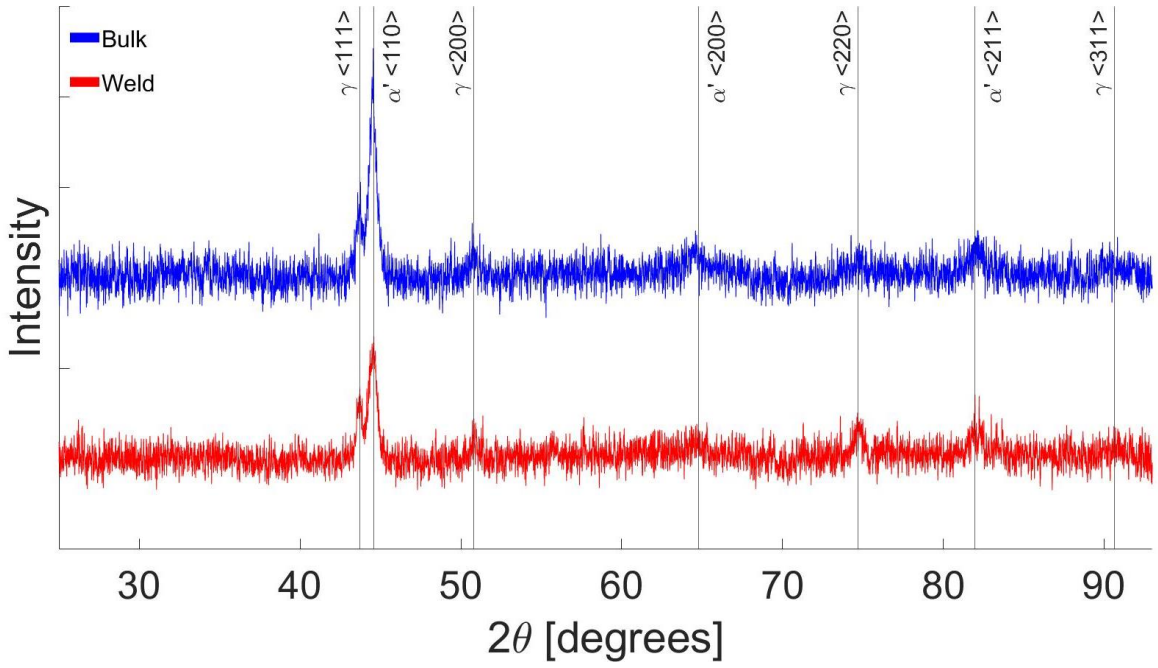


Figure 4.9 X-Ray diffraction data of bulk and weld material post-tensile test.

# Chapter 5: Discussion

## 5.1 Mechanical property evolution

While the values for the yield strength and ultimate tensile strength from the tensile tests are close between the bulk material and the welded sample, the elongation is a much more interesting topic. The mere presence of the weld in the specimen allowed the bulk material to stretch further than the unwelded sample. Indeed, the measurement of the yield strength is limited to the lesser of the two materials in this tensile configuration because the extensometer will read a "yield" point when the weaker material reaches its own yield strength. Since the tensile test cannot separate the strain responses of the two materials from each other, whichever material reaches its yield strength first is presented in the plot. This same principle also applies to the ultimate tensile strength.

As mentioned in section 4.1, the welded specimens ruptured in the bulk material far away from the weld zone. Again, this can be seen in Figure 4.1. This is due to the fact that after the welding procedure the molten steel recrystallized to form smaller grains than the bulk material as observed in the SEM and optical microscopy. Smaller average grain size is known to strengthen a material, and harden it, by increasing the number of grain boundaries; as grain boundaries interrupt dislocation propagation [34]. The smaller grains caused the weld to be harder than the bulk material and thus have a higher yield strength as well. This relationship between hardness and yield strength is a topic explored in a book by Was [17]. As the specimens were strained, the bulk material began to plastically deform before the weld material reached its yield point. At a given applied load at which both the weld and bulk materials are plastically deforming, the bulk material will experience a higher strain than the weld material.

The inflection points in the stress vs. strain curves of the unwelded samples associated with the change in strain-hardening do not appear in the welded samples. In the study by Byun et al., they propose that the increase in strain-hardening is due to martensite transformation [6]. The study by De and Speer also explains that the increase in strain-hardening in their experiments was due to the formation of α'-martensite [3]. They also explain the initial drop in strain-hardening in the lower portion of the plastic zone is associated with the formation of ε-martensite. From our experiments, we know that the tensile tests resulted in α'-martensite forming at a lower percentage in the weld than in the bulk material. This suggests that the weld experienced a lower level of strain than the bulk material since the amount of α'-martensite formed is directly tied to the amount of strain induced. The suppression of the α'-martensite phase formation within the weld caused a discontinuity along the sample. A possible consequence of this discontinuity was a limited propagation of twinning. These two phenomena had the effect of lowering the strain-hardening rate.

The hardness data showed that due to the tensile test, the bulk material of the welded sample strain hardened more than the material in the weld zone. The difference in the average hardness of the bulk material before and after the tensile test was 3.16 GPa, while the difference in the weld material was 2.50 GPa. Since hardness increases with applied strain, this again agrees with the claim that the bulk material experienced a higher strain than the weld during the tensile test.

## 5.2 Microstructure changes due to laser welding

### 5.2.1 *Phase changes and structure*

Recall that in the study by Yan et al., both δ-Fe and γ-austenite were present in 304 laser welded joints. The laser welding in that study was done at a rate of 16.67 mm/s with a peak power of 4 kW. The settings for our weld were 3.17 mm/s at a peak power of 2 kW. The thicknesses of the 304 being welded were 3 mm for Yan et al. and 1.52 mm for ours. Compared to their settings, our weld speed was more than 5 times slower and material thickness half. The heat energy added to our samples potentially was much different per unit mass. This could have led to a slower cooling rate, which allowed the δ-Fe to transform completely into γ-austenite in our pre-tensile test sample. According to both Yan et al. and Kumar et al., high cooling rates in stainless steels leads to more δ-Fe in the final material [14, 16]. However, Yan et al. state that slower cooling rates leads to larger grain sizes, which our weld did not have. Potentially the weld parameters used for the present study struck a balance in these cooling rates to produce small grains and fully transform the δ-Fe to γ-austenite.

### 5.2.2 *Correlation with mechanical properties*

Using the difference in nanohardness between the bulk material and the weld pre-tensile test, a difference in the yield strength can be predicted [17]. The difference in the average nanohardness values from section 3.2 is equal to $\Delta H_{nano}$ = 408.19 MPa. By taking the geometry of the indent into account, this value can be converted into a difference in Vickers hardness of [35]:

$$\Delta H_{Vickers} = 0.0945 \times \Delta H_{nano} \quad (5.1)$$

$$\Delta H_{Vickers} = 38.57\ kgf/mm^2 \quad (5.2).$$

Using the correlation between hardness and yield strength in (5.3) for an austenitic steel from [17], the difference in hardness can be expressed as a difference in yield strength as

$$\Delta\sigma_y = 3.03 \times \Delta H_{Vickers} \quad (5.3)$$

$$\Delta\sigma_y = 116.88\ MPa \quad (5.4).$$

This $\Delta\sigma_y$ can then be used in the Hall-Petch relation in (5.5) in order to estimate the change in the grain size between the welded zone and the bulk material away from the weld [36]. This relation hypothesizes that the difference in yield strength between the bulk and weld materials is entirely due to the difference in grain size.

$$\sigma_y = \sigma_i + k_y d^{-1/2} \quad (5.5)$$

According to Xue et al., for a 304 stainless steel the parameters of (5.5) are $\sigma_i$ = 163.8 MPa and $k_y$ = 0.75 MPa*m$^{1/2}$ [37]. Evaluating (4.5) for both the weld and the bulk independently by introducing the yield stress values of $\sigma_y$ = 290 MPa and $\sigma_y$ = 290 + 116.88 = 406.88 MPa, respectively, returns a difference in grain diameter of $\Delta d$ = 25.8 μm required if the difference in hardness was entirely due to the grain size effects.

The values for this $\Delta d$ as determined by the grain size computation methods in section 4.3 are $\Delta d$ = 6.32 μm for the optical microscopy and $\Delta d$ = 7.42 μm for the SEM. These values are far from the hypothesis stated from Hall-Petch relation using the nano-indentation data. This means that the Hall-Petch relation does not describe the hardening mechanism properly in this case. In a study by Mao et al., the hardness relation between a 304L base metal welded with a 308L filler material was investigated [23]. They also discovered that the Hall-Petch relation did not solely explain the difference in hardness between the weld and the bulk material. They created a mathematical model that predicted the change in hardness within ±10% by taking into account the change in grain size, solid solution, dislocations, and precipitates. These are also factors that may influence our sample.

Returning to the hardness results of the welded sample, the changes in the yield strengths associated with the changes in hardness are 904.82 MPa and 715.84 MPa for the bulk and the weld respectively. If a metal's behavior during a strain – total relaxation – strain sequence is considered, the maximum stress experienced by these materials during the tensile test could be approximated using the increase in hardness. Since a metal's strain response upon reloading after a total relaxation follows the elastic modulus up to the previously experienced maximum stress, effectively a new yield strength is created. The increase in yield strengths mentioned here could be applied to find the maximum applied stresses of the materials. These would be 1,194.82 MPa and 1,122.72 MPa for the bulk and the weld respectively. A general assumption during tensile testing is that the cross-sectional area is constant throughout the gauge length of the specimen until necking occurs; this means that the stress must also be constant regardless of material. These two values are within approximately 6% of each other, which is consistent with this assumption. Visually, the weld on the tensile tested specimens appears to be wider and thus maintained a larger cross-sectional area than the bulk material. This would be the source of the lower maximum stress in the weld than the bulk stated here. This difference in cross-sectional area could be explained by the Poisson's ratio, $\nu$, of the material in

$$\nu = -\frac{\epsilon_{transverse}}{\epsilon_{axial}} \quad (5.6).$$

The Poisson's ratio of 304 stainless steel is generally considered to have a value of 0.305 [38]. As the material is strained axially, the cross-sectional area is reduced. Since the cross-sectional area of the weld did not reduce as much as the bulk, it must have experienced a lower strain.

The elongation of the weld could also be approximated using the nanohardness data. The length of the weld before tensile testing was 1.80 mm, and after tensile testing it was 2.40 mm long. This equates to an elongation of 0.60 mm, or an engineering strain of 33%. Considering that the total gauge length before the tensile test was 25.4 mm less the 1.80 mm of the weld, the total length of bulk material was 23.6 mm. The total elongation of specimen 3 during the tensile test was 18.11 mm, less the elongation of the weld of 0.60 mm, the elongation of the bulk must have been 17.51 mm, or 74.20% engineering strain.

## 5.3 Modeling

### 5.3.1 *Finite Element Analysis*

Using the information discovered from the hardness and tensile testing in a finite element analysis (FEA) model the material properties of the weld were further deduced. A systematic approach and a simplified model of the stress vs. strain curves of the specimens were used to achieve this.

To begin, a solid model was created to the specifications described in Figure 2.5. This model comprised of three solid bodies representing the upper bulk section, the weld section, and the lower bulk section. The middle section represents a simplified model of the weld as a rectangular shape. Even though there is no weld in specimen 1, the same three-body model needed to be used throughout the simulation to maintain mesh consistency. This model is shown in Figure 5.1. The approach of this experiment was to run the simulation using material properties found from the tensile tests of specimens 1 and 4 on the model with all three bodies having the same material properties. The second step was to apply the material properties from specimen 1 to the upper and lower "bulk" solid bodies of the model and apply approximated material properties from the physical tests to the middle "weld" solid body until the simulations response approximately matched the response of the simulation of the welded specimen 4.

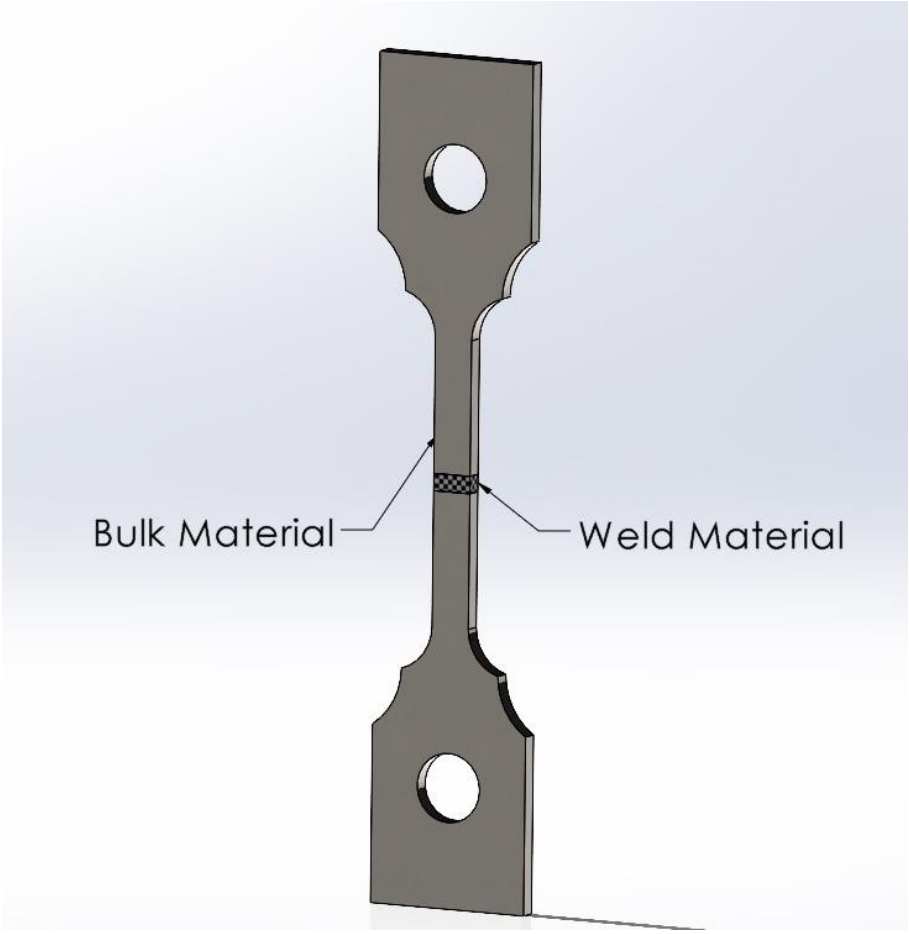


Figure 5.1 The SolidWorks model used for the FEA analysis. The image shows the weld with a hatched pattern in the center of the solid model.

The SolidWorks Simulation model was set up to mimic the physical tensile tests of the welded and unwelded specimens. The following conditions were applied to all simulations. The surface of the lower hole was set with a fixed boundary condition while a force of 4000 N was applied to the upper hole in the lengthwise direction creating a tensile load on the specimen. A bearing boundary condition on the lower hole could have given a more accurate method, but a fast solve time was prioritized. Regardless, the area of interest is the gauge section, and the boundary conditions of the holes would have little effect on the gauge section. The force of 4000 N was chosen because it is close to, but still lower than the maximum load that the Instron tester applied to any of the four specimens. This is important because the simulation cannot solve if the material reaches its ultimate tensile strength as the material would rupture at that point. Bonded contacts were used at the interfaces of the solid bodies. The mesh was set to a size of 0.99 mm to ensure at least two elements across the thickness of the part. An extra mesh control of 0.4 mm was applied to the edges between

the solid bodies to create four elements across the length of the weld. The generated mesh of the model is shown in Figure 5.2.

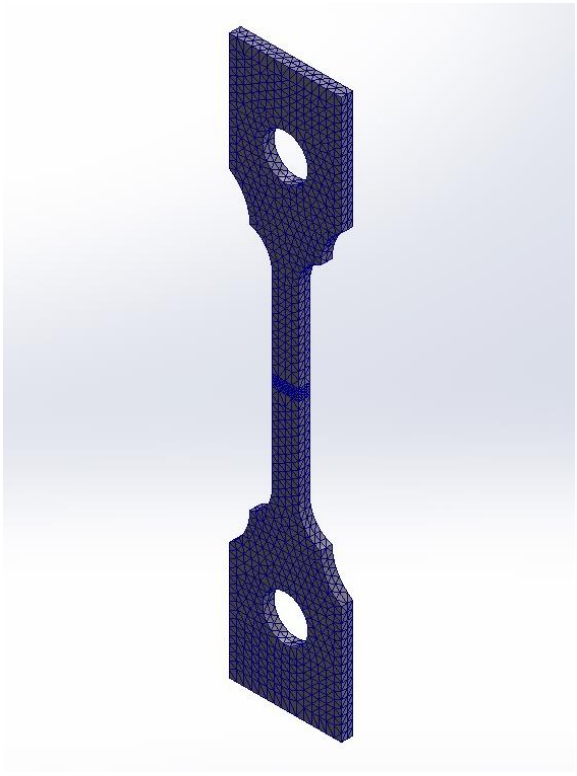

Figure 5.2 The generated mesh on the model with three solid bodies.

SolidWorks Simulation has the ability to solve finite element analysis problems with user-defined material properties including for plastic deformation. Two methods for inputting plasticity data were considered for this simulation. The first is to import actual data points of the plastic region of a stress-strain curve. This method uses the material properties such as elastic modulus and yield strength for the linear elastic region. If the simulation reaches the yield strength it uses the user-input stress-strain data points to calculate the deformation. The second method for plastic deformation is to define the elastic modulus and yield strength as before but also a so-called tangent modulus. The tangent modulus ($T_M$) is the slope of a linear approximation of the plastic region of the true stress-true strain curve. This gives a relation between the true strain and true stress of a material as follows in

$$\sigma_{true} = \begin{cases} E\epsilon & for\ \sigma < \sigma_y \\ T_M\epsilon & for\ \sigma > \sigma_y \end{cases} \quad (5.7).$$

The choice was made to move forward with the latter method. This was because it would require a simpler method of approximating the stress strain curve of the weld later. The results would not predict the real-world results accurately, but that is less important than to compare the results of the simulations. This method requires the approximation of the empirical stress-strain curves into a

bilinear function. The first region of the function has the slope equal to the elastic modulus of the material up to the yield strength. The second region has a lower slope up the ultimate tensile strength. For the simulations of specimens 1 and 4 the nominal value of 195 MPa was used for the elastic modulus while 290 MPa was used for the yield strength. A linear curve was fit to the plastic regions of specimens 1 and 4 to find the tangent modulus of each. These were found to be 2174 and 1830 MPa respectively. A Von-Mises plasticity model was used for all simulations. Figure 5.3 shows the resulting engineering stress vs. engineering strain curves from the physical tensile tests of specimens 1 and 4 overlayed with the approximated curves using the tangent moduli. Figure 5.3 (a) shows these curves for Specimen 1 while (b) shows these curves for Specimen 4. This shows that the tangent modulus curves maintain approximately the same slope of the actual curves but are slightly offset due to not having a transition in the slope after the yield point. The tangent modulus curves maintain the ultimate tensile strength from the experimental data.

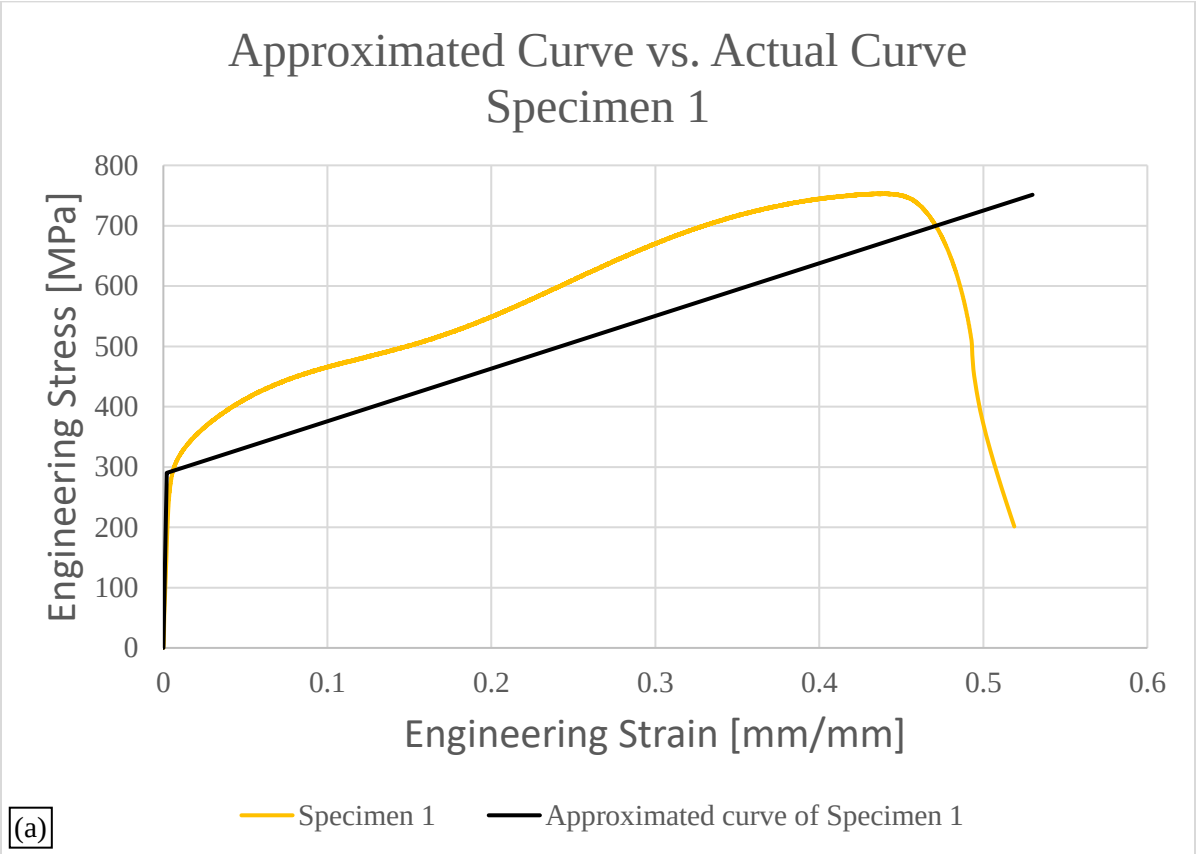
Approximated Curve vs. Actual Curve
Specimen 1
Engineering Stress [MPa]
800
700
600
500
400
300
200
100
0
0
0.1
0.2
0.3
0.4
0.5
0.6
Engineering Strain [mm/mm]
Specimen 1
Approximated curve of Specimen 1

(a)

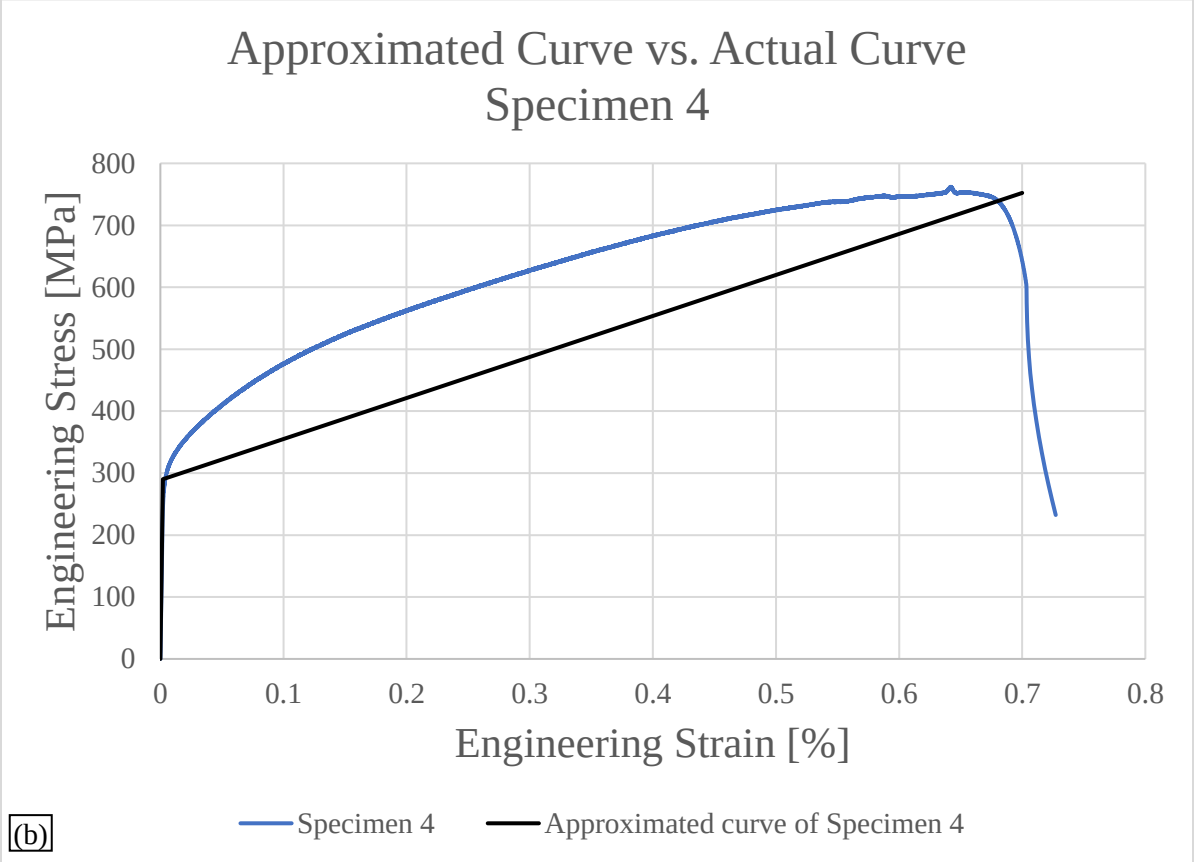


Figure 5.3 The approximated stress-strain curves overlayed with the experimental data from the tensile tests of specimens 1 and 4.

The simulation was performed for each specimen material and the elongation of the gauge section was recorded. These were 9.73 and 12.3 mm respectively. These correspond to engineering strain values of 37.9% and 48.4%. These were not expected to exactly match the actual strain values of the tensile tests since the simulation did not continue until fracture and the strain response was a coarse approximation. With 4000 N corresponding to a stress of about 740 MPa in the specimen, these strain values are near the expected strain values from the tensile test. The next step was to apply the material properties used for specimen 1 to the upper and lower 'bulk' solid bodies and create a new material for the middle 'weld' section. The properties for this new material were found using the physical tests in this study.

The yield strength of the weld was found using the $\Delta\sigma_y$ = 116.88 MPa found in (4.4). Using $\sigma_{y,bulk}$ = 290 MPa for the bulk material, $\sigma_{y,weld}$ = 406.88 MPa. The lengths of the weld before and after tensile testing were physically measured with calipers to find the strain induced in the weld. These measurements were 0.05 inches and 0.06 inches respectively, giving an engineering strain of 20%. The relaxation of the material after the tensile test also needed to be taken into consideration. This

relaxed state is the length measured by the calipers. Knowing the yield strength, applied strain, that the relaxation rate is the same as the elastic modulus, and that the weld experienced the same maximum stress as the ultimate tensile strength of the tensile test, the tangent modulus can be found. This is done by simply connecting the dots. Figure 5.4 shows this method represented on a stress-strain plot. The tangent modulus found using this method was 4131 MPa. This method does lack accuracy but can be repeated without special equipment.

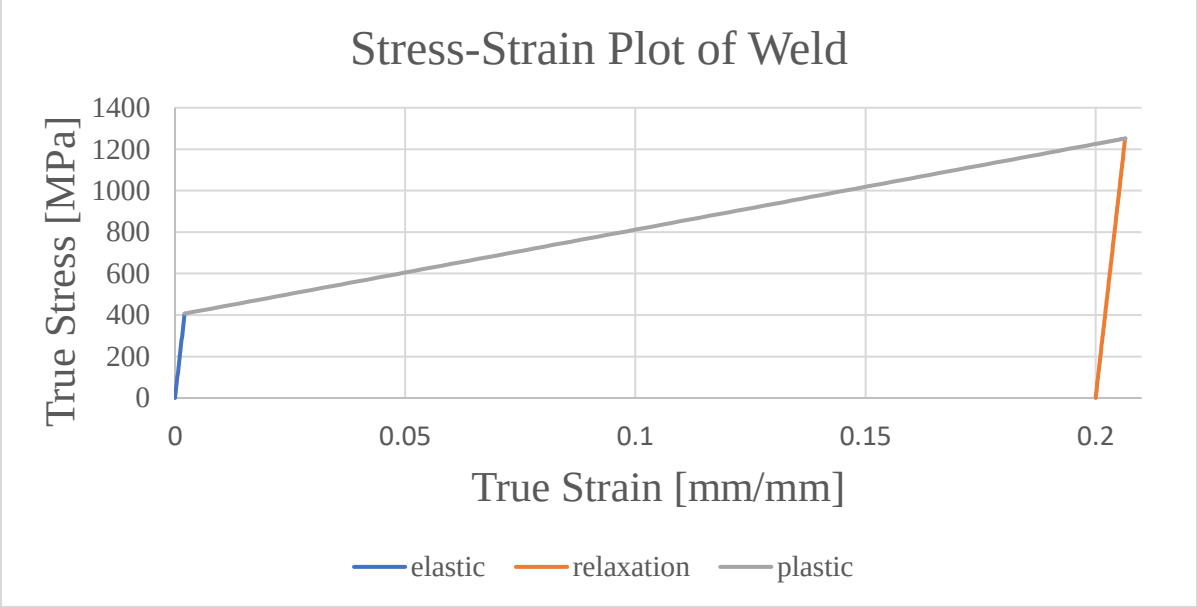


Figure 5.4 The approximated stress-strain plot of the weld material by using the tangent modulus found with the caliper measurement.

Two other methods were used to find the induced strain of the weld. For the first of these, the hardness profiles from the nanoindentation experiments were used. By finding the regions associated with the weld in this data, the weld was determined to be 1.80 mm long before the tensile test and approximately 2.40 mm long after the tensile test, giving an engineering strain of 33%. This was used in the same method as shown in Figure 5.4 to find the tangent modulus. This was found to be equal to 2508 MPa. This method is subject to interpretation of the nanoindentation data and is also limited by the resolution of the indent spacing. In other words, because the indent spacing was 150 µm, and the initial length of the weld was 1.8 mm, the calculated induced strain could be ±8.33% of the actual value. The gradual changes of hardness values in the data makes it difficult to define where exactly the weld material begins and ends.

The final measurement method was to compare the width of the welds before and after the tensile testing under a microscope. Using a microscope the distinction between weld and bulk material becomes much more clear than using the previous two methods. An image of the two welds

taken with an Amscope MU2003-BI microscope digital camera under 5X magnification is shown in Figure 5.5. Since the tensile test caused the sample to “bow”, it did not lay flat next to the non-tensile-tested sample on the microscope stage. This made it impossible to bring both samples into focus at the same magnification. This would be a source of error in the measurement. Using this measurement method the weld was determined to stretch approximately 57% of its original length, which gives a tangent modulus of 1472 MPa using the same graphing method as before. The values for the apparent strain and resulting tangent moduli from these three measurement methods are shown in Table 5.1. Clearly, these measurements have a wide variance. Each method has its own advantages and drawbacks and could be used depending on available resources.

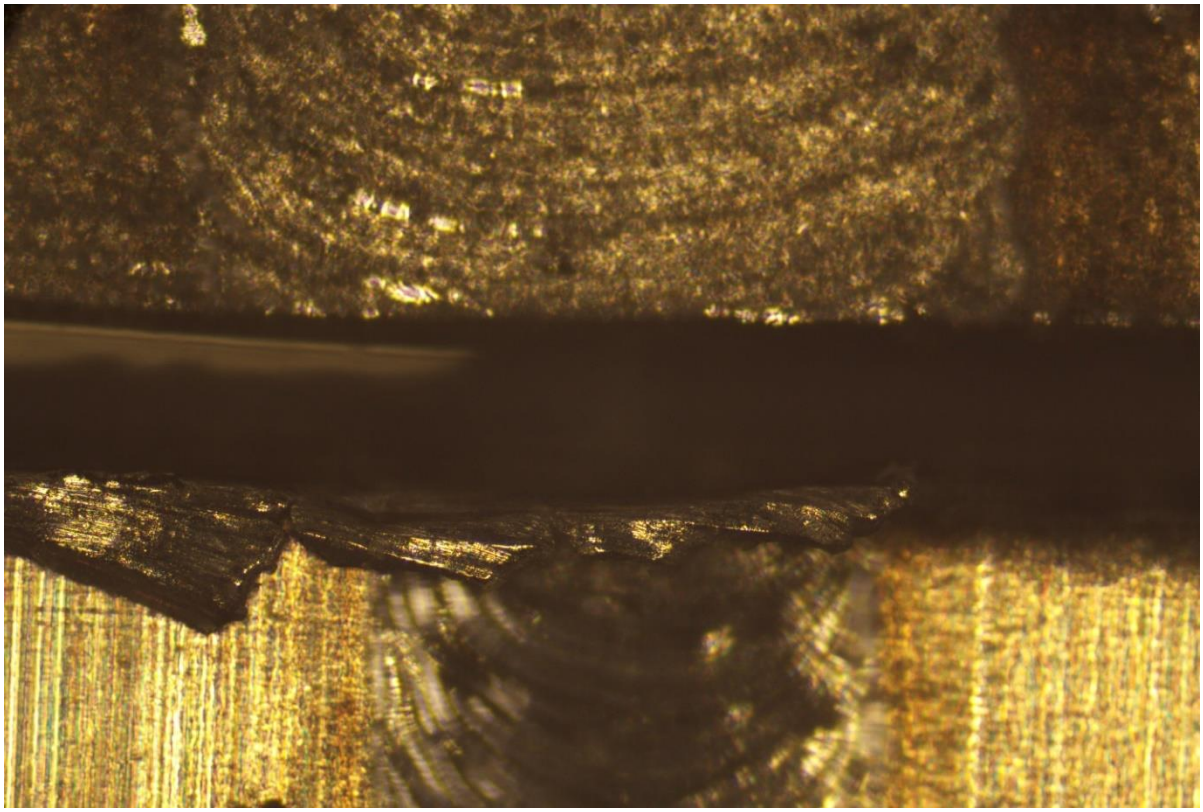

Figure 5.5 A comparison of the laser weld before and after the tensile test. The upper portion of the image is the tensile tested weld specimen 3 and the lower portion is the untested weldment.

The tangent modulus value of 4131 MPa from the caliper measurement was used as a starting point for the material properties of the weld in the SolidWorks Simulation. The rounded value of 407 MPa was used for the yield strength of the weld and 195 MPa was used for the elastic modulus. These properties were applied to the middle ‘weld’ section of the model while the properties from specimen 1 were applied to the upper and lower sections of the model. The same boundary conditions and loads were applied as before. The elongation resulting from these parameters was 9.95 mm, this correlates

to an engineering strain of 39.2%. Clearly, these results do not match the results of the simulation of the homogeneous specimen 4. This same procedure was repeated for the tangent modulus values determined from the other measurement methods. The engineering strain values for the tangent moduli from the hardness and microscope measurements are 40.2% and 44.0% respectively. The resulting elongation and strain values are shown in Table 5.1.

Table 5.1 The resulting elongation and strain values from the simulation using tangent modulus values derived from calipers, hardness profile, and microscope measurements.

| **Measurement method** | **Tangent modulus of the weld [MPa]** | **Elongation [mm]** | **Engineering strain [%]** |
|---|---|---|---|
| **Microscope** | 1472 | 11.18 | 44.0 |
| **Hardness Profile** | 2508 | 10.21 | 40.2 |
| **Calipers** | 4131 | 9.95 | 39.2 |

The results of the models with custom weld material properties did not match the results of the model of specimen 4 perfectly. The results from the microscope measurement were the closest, within 5% strain of the specimen 4 simulation. Considering there is a difference of only 10% strain between the specimen 1 and specimen 4 model results, this is a significant error. This suggests the notion that the laser weld introduced some discontinuity in and altered the strain response of the bulk material. The FEA examination focused on changing only the weld material properties. Because the material properties of the bulk material were not changed, it shows that the weld itself did not increase the ductility of the specimens. Determining the elongation that the weld would need to experience to fully account for the difference between the welded and unwelded samples can further support this. The unwelded specimen 1 stretched 51.6%, or to a final length of 38.5 mm. The welded specimen 4 stretched 72.5%, or to a final length of 43.8 mm. This means the specimen 4 stretched 5.3 mm further than specimen 1. The weld was initially 1.8 mm in length, and a 1.8 mm section of the unwelded specimen 1 would have stretched 0.93 mm during the tensile test. If the 1.8 mm weld replaced this 1.8 mm section of bulk material, it needs to make up the difference of 5.3 mm of extra elongation in specimen 4. Combine this with the elongation of the 1.8 mm section of bulk material of 0.93 mm, the weld section would need to stretch 7.23 mm during the tensile test. This would mean a strain value of 402%! This is contrary to traditional wisdom that says when a metal is welded, the weld material is harder and stiffer than the bulk material. The weld did not stretch this much as is

evident that none of the physical measurements came close to this value. A sketch of this comparison is shown in Figure 5.6.

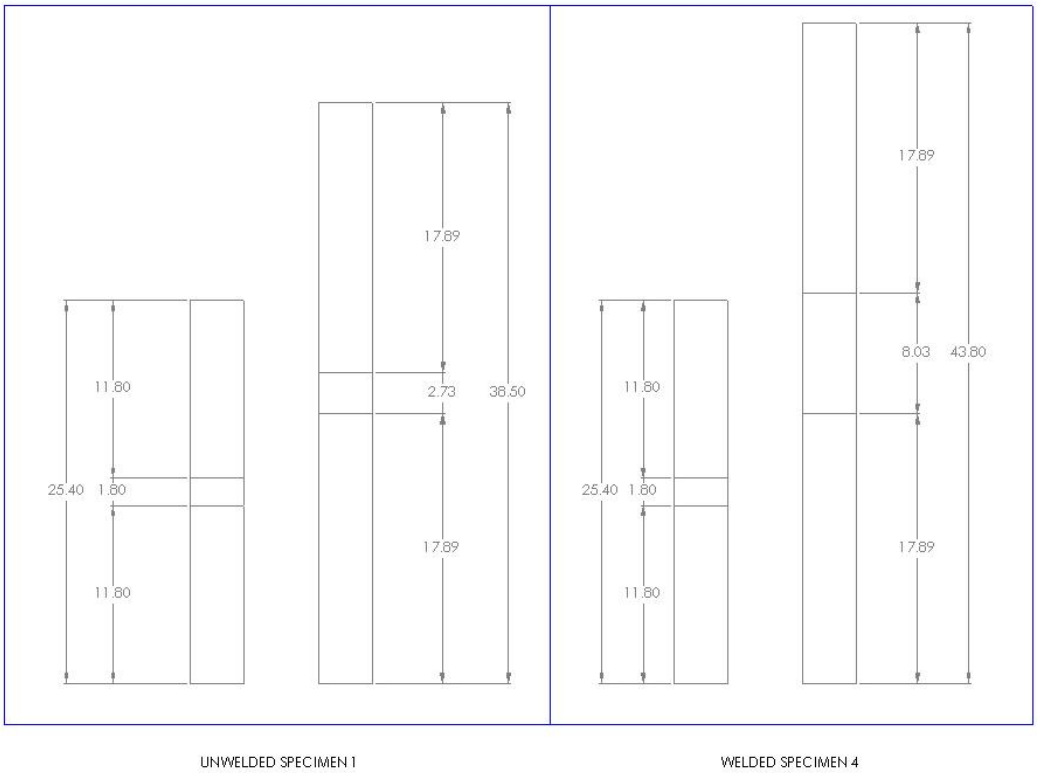


Figure 5.6 A comparison of the elongation of specimen 1 (left) and the theoretical elongation of specimen 4 during the tensile test (right).

### 5.3.2 *Strain-hardening exponent*

Another method of modeling the stress-strain curve of a material is to use the strain hardening exponent approximation, also known as Holloman's Equation. This approximates the strain response of a material as a linear relation in the elastic region and a power relation in the plastic region. This is described in

$$\sigma = \begin{cases} E\epsilon & \epsilon \leq \epsilon_{ys} \\ K\epsilon^n & \epsilon > \epsilon_{ys} \end{cases} \quad (5.8),$$

where $\sigma$ is the true stress, $n$ is the strain hardening exponent, $E$ is the elastic modulus, $\epsilon$ is the true strain, and $K$ is the strength coefficient and is defined in

$$K = E^n \sigma_{ys}^{1-n} \quad (5.9),$$

where $\sigma_{ys}$ is the yield strength.

A method of relating this strain hardening exponent to the hardness of a material is shown in

$$\frac{H}{\sigma_r} = f\left[\frac{2}{3}\left(\frac{\epsilon_{ys}}{0.1}\right)^n + \theta(n) + M(n)\left(\frac{z_{ys}+1.217a_s}{a_s/_{0.635}}\right)^{P(n)}\right] \quad (5.10),$$

proposed by Mata et al. [39]. It is used for materials whose strain response is plastically dominated. In this equation $H$ is the hardness, $\sigma_r$ is the uniaxial stress, $f$ is the probe geometry projection factor specific to the indenter tip, $z_{ys}$ is the depth of the plastic zone, and $a_s$ is the contact radius of the indenter. For our nanoindentation test we used a Berkovich indenter tip which has an associated $f$ factor of 1.101. According to Mata, the uniaxial stress is defined such that for any material whose contact response (to the indenter) is plastically dominated

$$\frac{H}{\sigma_r} = 2.7 \quad (5.11).$$

For this analysis $z_{ys}$ in (5.10) was assumed to be equal to 5 times the indent depth. The value for $\varepsilon_{ys}$ was found using the nominal value of 195 MPa for the elastic modulus and a 0.2% yield offset. $\Theta(n)$, $M(n)$, and $P(n)$ are functions of the strain hardening exponent as defined by the following Equations:

$$\theta(n) = 2.5968 + \frac{0.5097}{n} \quad (5.12),$$

$$M(n) = -2.2778 - \frac{0.5479}{n} \quad (5.13),$$

and

$$P(n) = -3.0615n - 0.005 \quad (5.14).$$

According to Mata et al., normalized plastic zone sizes are equivalent for round-tipped indenters and Berkovich indenters when the contact radius of the Berkovich tip is measured at 25° from the indenter tip edge from the indenter tip to the outer-most contact point with the material. This is shown in Figure 5.7. The contact radius of the Berkovich tip was determined for the final

nanoindentation depth of 3000 nm to be 7187 nm.

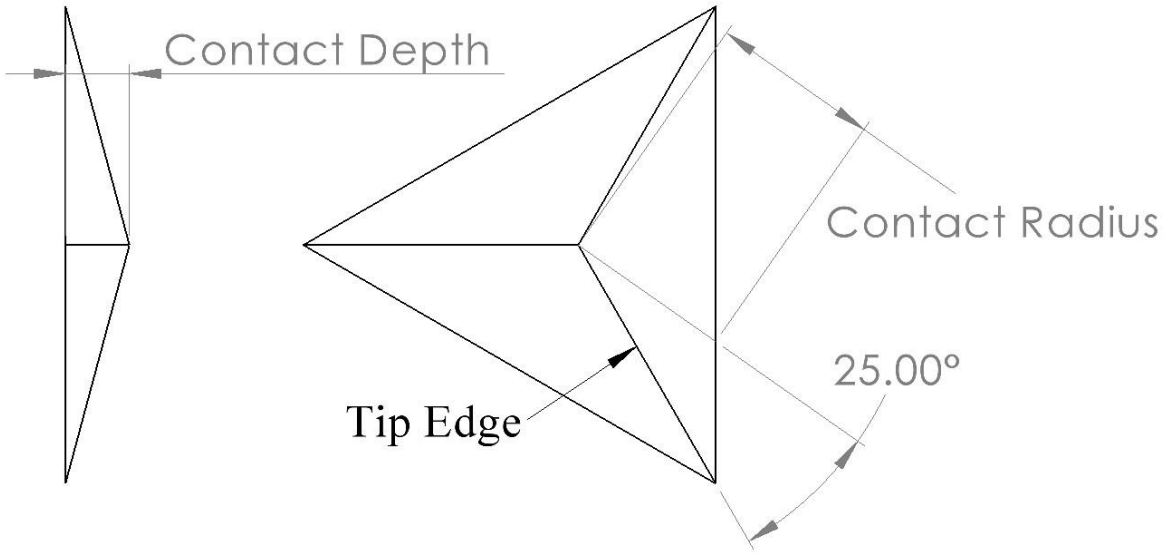


Figure 5.7 The contact radius as of the Berkovich indenter tip.

Using the information described and the average hardness values from the pre-tensile test data in section 5.2, (5.10) was solved for the strain-hardening coefficient *n* using an iterative technique for both the weld and the bulk materials. The *n* values of 0.278 and 0.287 were calculated for the weld and the bulk respectively. (4.8) was plotted using both of these *n* values as shown in Figure 5.8. This Figure also shows a comparison of the strain hardening exponent model to the tangent modulus approximation from section 5.3. Notice here that the *n* value for the weld is lower than that of the bulk, but the weld curve on the graph is higher than that of the bulk. This is due to the strength coefficient *K* as defined in (4.9). Because the yield strength and the value for *1-n* is higher for the weld than the bulk, the overall *K* is higher. Since *K* is a multiplier in the equation this causes the weld curve to be higher than the bulk curve. The *K* values are 2263 and 1879 MPa for the weld and bulk respectively using the values of 407 and 290 MPa for the yield stresses.

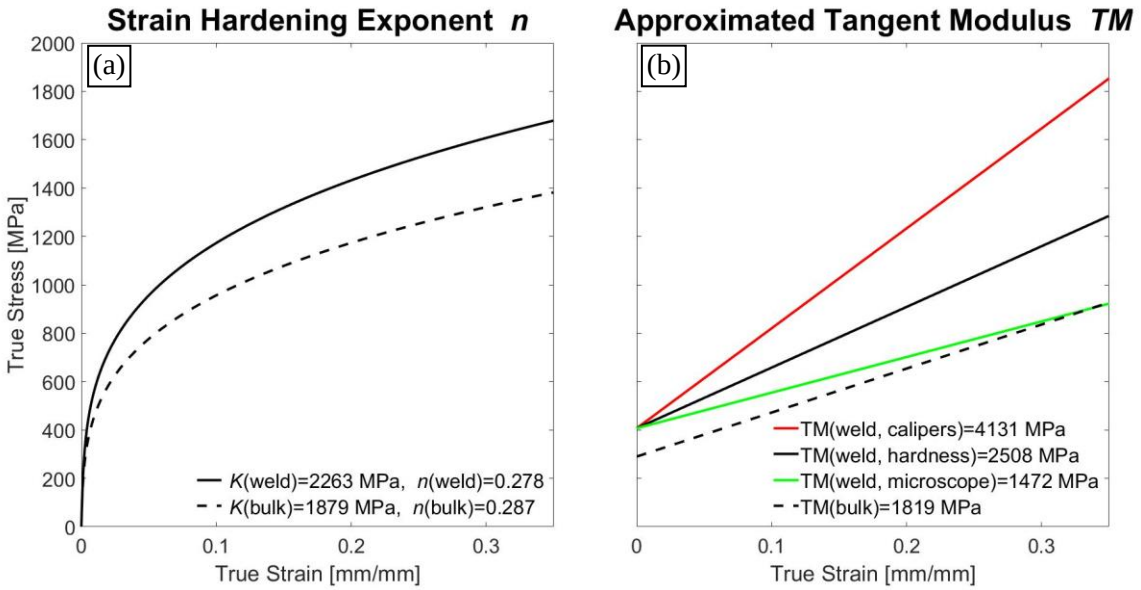


Figure 5.8 (a): The plot showing the strain hardening curves of the weld and the bulk; (b): The plot showing the tangent modulus values of the weld from the three different measurement methods and of the bulk.

A trend in the strain hardening exponent graph is that the weld curve is higher and steeper than the bulk curve. In the tangent modulus graphs this is also true for the curves using the calipers (solid red line) and the hardness (solid black line) measurements. The curves for the hardness measurement and the bulk are nearly parallel, but the weld curve is still steeper. The slope of the microscope (solid green line) curve is lower than that of the bulk. On this chart, these two curves intersect at approximately 900 MPa true stress. So, for any applied true stress above 900 MPa on this curve. In contrast, the other two measurement curves have steeper tangent moduli so will always experience a lower strain than the bulk at any given applied stress.

The stress-strain curve for the weld material was able to be approximated using the information gathered from the results of several physical tests on welded and unwelded samples of this 304 alloy. Through each physical test that was performed in this study, important information on the behavior of the weld was discovered. The initial tensile test showed that the welded sample provided more ductility, eliminated the strain hardening inflections, and maintained the same ultimate tensile strength of the unwelded sample. The first nanoindentation test on the pre-tensile tested sample showed that the weld did in fact produce a harder material than the bulk and offered a higher yield strength. The bulk material had an average hardness of 2.10 GPa while the hardness of the weld was 20% higher at 2.51 GPa. The microscopy analysis provided the grain sizes of both the bulk and the weld pre-tensile test. These showed that the weld had a smaller average grain size than the bulk. Using the results of the microscopy and the pre-tensile test nanoindentation showed that the Hall-

Petch relationship did not explain the increase in hardness and that other strengthening factors contributed. The post-tensile test nanoindentation results showed that the bulk experienced a higher amount of strain-hardening than the weld material did during the tensile test. This is because the increase in hardness after the tensile test was higher for the bulk than the weld. The post-tensile test average hardness values were 5.26 and 5.01 GPa and increases of 3.16 and 2.50 GPa for the bulk and the weld respectively. The x-ray diffraction provided the microstructure phase of the weld material pre-tensile test and the weld and the bulk materials post-tensile test. This showed that the weld was initially purely austenitic. These results also correlated with the nanoindentation results showing that the bulk material experienced a higher strain than the weld during the tensile test because it contained a higher martensite fraction than the weld. Using these results of the physical tests and measuring the induced strain of the weld due to the tensile test, along with the assumption that the weld material has the same elastic modulus as the bulk material, an approximate stress-strain curve of the weld was produced.

# Chapter 6: Conclusion

## 6.1 Conclusions

A commercially laser welded alloy of 304 stainless steel was the subject of this study. Tensile tests of the base 304 alloy were compared to tensile tests of the laser welded sample. The laser welded sample maintained the same ultimate tensile strength while gaining ductility. The material properties of the weld material were approximately determined using optical and scanning electron microscopy, XRD, and nanoindentation. Finally, those properties were tested in an FEA simulation and compared to a strain hardening exponent model. The following conclusions can be made from this study:

1. Industrial laser welding of 304 SS produced a joint with an estimated yield strength of 407 MPa inside the weld zone, significantly higher than the unwelded bulk material which has a yield strength of approximately 290 MPa.
2. The increase in yield strength is partially attributed to smaller average grain sizes observed within the weld zone of the joint, which is only 1.8 mm wide. This weld zone appears to retain the austenitic structure consistent with the bulk 304 SS material.
3. During tensile testing, the welded samples fractured away from the weld region in the bulk material maintaining the same ultimate tensile strength as the non-welded samples, while experiencing a substantial improvement in ductility (from ~53% to ~72%). This increase in ductility is attributed to suppressed formation of strain-induced alpha phase (within the weld) and limited propagation of strain-induced twinning throughout the sample.
4. Although prior to the tensile test the material inside the weld zone had a higher hardness than the material outside, the tensile test resulted in a 27% larger increase in hardness in the bulk than the weld material. This, along with x-ray diffraction analysis, showed that the weld zone experienced less strain hardening than the bulk material of the welded sample during the tensile test.
5. Using the results of the tests performed in this study and taking measurements of the stretch of the weld zone due to the tensile test, a reasonable simulation of the strain response of the weld zone was created using simple finite element analysis techniques.

## 6.2 Recommendations for future work

This project was limited in scope by time and resources. More experiments would add valuable information to the results. My recommendations for these are as follows:

1. Performing an x-ray diffraction analysis on the bulk 304 sample as received from the mill. This would provide the baseline phase for the bulk material to compare with the post-tensile test XRD results. As of now, it was assumed that the bulk material was purely austenitic just

as the weld was, but this steel was cold-rolled at the mill and an XRD would show how much strain-hardening was applied by this process. These results would then allow the comparison of the changes in martensite between the bulk and the weld materials due solely to the tensile test.

2. We found that the Hall-Petch relationship did not fully explain the change in hardness between the weld and the bulk material pre-tensile test. Studying other factors such as precipitates, dislocations, and solid solution would give a more thorough understanding of the changes the welding procedure had on the base material. One could then use the results of these in the Mao analysis.
3. Finally, finding the ultimate tensile strength of the weld itself will allow for a more precise approximation of the stress-strain curve of the weld material. Currently, the value of the ultimate tensile strength was assumed based off the other points of the stress-strain curve. Creating a new tensile sample geometry with the smallest cross-sectional area at the location of the weld and a very low stress concentration factor at that point would force the specimen to rupture at the weld. This would make the ultimate tensile strength of the weld show itself in the resulting stress-strain curve.

# Bibliography

[1] AMERICAN SOCIETY FOR METALS (ASM), *Engineering properties of steel*. AMERICAN SOCIETY FOR METALS (ASM), 1982.

[2] E. Medina, J. M. Medina, A. Cobo, and D. M. Bastidas, "Evaluation of mechanical and structural behavior of austenitic and duplex stainless steel reinforcements," *Construction and Building Materials*, vol. 78, pp. 1–7, Mar. 2015, doi: 10.1016/j.conbuildmat.2015.01.008.

[3] A. K. De and J. G. Speer, "Deformation-Induced Phase Transformation and Strain Hardening in Type 304 Austenitic Stainless Steel."

[4] X. T. Deng, M. Cheng, S. H. Zhang, H. W. Song, and M. A. Taha, "Residual stresses and martensite transformation in AISI 304 austenitic stainless steel," *Materials Research Express*, vol. 6, no. 1, Jan. 2019, doi: 10.1088/2053-1591/aae292.

[5] C. Celada-Casero, H. Kooiker, M. Groen, J. Post, and D. San-Martin, "In-situ investigation of strain-induced martensitic transformation kinetics in an austenitic stainless steel by inductive measurements," *Metals (Basel)*, vol. 7, no. 7, Jul. 2017, doi: 10.3390/met7070271.

[6] T. S. Byun, N. Hashimoto, and K. Farrell, "Temperature dependence of strain hardening and plastic instability behaviors in austenitic stainless steels," *Acta Materialia*, vol. 52, no. 13, pp. 3889–3899, Aug. 2004, doi: 10.1016/j.actamat.2004.05.003.

[7] G. C. Soares, M. C. M. Rodrigues, and L. de Arruda Santos, "Influence of temperature on mechanical properties, fracture morphology and strain hardening behavior of a 304 stainless steel," in *Materials Research*, 2017, vol. 20, pp. 141–151. doi: 10.1590/1980-5373-mr-2016-0932.

[8] A. Y. Chen *et al.*, "The influence of strain rate on the microstructure transition of 304 stainless steel," *Acta Materialia*, vol. 59, no. 9, pp. 3697–3709, May 2011, doi: 10.1016/j.actamat.2011.03.005.

[9] G. C. Soares, B. M. Gonzalez, and L. de Arruda Santos, "Strain hardening behavior and microstructural evolution during plastic deformation of dual phase, non-grain oriented electrical and AISI 304 steels," *Materials Science and Engineering A*, vol. 684, pp. 577–585, Jan. 2017, doi: 10.1016/j.msea.2016.12.094.

[10] J.-Y. Choi and W. Jin, “STRAIN INDUCED MARTENSITE FORMATION AND ITS EFFECT ON STRAIN HARDENING BEHAVIOR IN THE COLD DRAWN 304 AUSTENITIC STAINLESS STEELS,” 1997.

[11] Y. F. Shen, X. X. Li, X. Sun, Y. D. Wang, and L. Zuo, “Twinning and martensite in a 304 austenitic stainless steel,” *Materials Science and Engineering A*, vol. 552, pp. 514–522, Aug. 2012, doi: 10.1016/j.msea.2012.05.080.

[12] T. Lincoln Electric Company, “Stainless Steels Welding Guide,” 2003.

[13] A.-M. El-Batahgy, “Laser Beam Welding of Austenitic Stainless Steels – Similar Butt and Dissimilar Lap Joints,” in *Welding Processes*, InTech, 2012. doi: 10.5772/48756.

[14] J. Yan, M. Gao, and X. Zeng, “Study on microstructure and mechanical properties of 304 stainless steel joints by TIG, laser and laser-TIG hybrid welding,” *Optics and Lasers in Engineering*, vol. 48, no. 4, pp. 512–517, Apr. 2010, doi: 10.1016/j.optlaseng.2009.08.009.

[15] M. Alali, I. Todd, and B. P. Wynne, “Through-thickness microstructure and mechanical properties of electron beam welded 20 mm thick AISI 316L austenitic stainless steel,” *Materials and Design*, vol. 130, pp. 488–500, Sep. 2017, doi: 10.1016/j.matdes.2017.05.080.

[16] N. Kumar, M. Mukherjee, and A. Bandyopadhyay, “Comparative study of pulsed Nd:YAG laser welding of AISI 304 and AISI 316 stainless steels,” *Optics and Laser Technology*, vol. 88, pp. 24–39, Feb. 2017, doi: 10.1016/j.optlastec.2016.08.018.

[17] G. S. Was, “Fundamentals of radiation materials science: Metals and alloys, second edition,” *Fundamentals of Radiation Materials Science: Metals and Alloys, Second Edition*, pp. 1–1002, Jan. 2016, doi: 10.1007/978-1-4939-3438-6.

[18] L. Chen, T. Yang, Y. Zhuang, and W. Chen, “The multi-objective optimization modelling for properties of 301 stainless steel welding joints in ultra-narrow gap laser welding”, doi: 10.1007/s40194-021-01068-5/Published.

[19] S. B. Adisa, I. Loginova, A. Khalil, and A. Solonin, “Effect of laser welding process parameters and filler metals on the weldability and the mechanical properties of aa7020 aluminium alloy,” *Journal of Manufacturing and Materials Processing*, vol. 2, no. 2, 2018, doi: 10.3390/jmmp2020033.

[20] G. Zhang and F. Yu, “Ultra-Narrow Gap Fiber Laser Conduction Welding Technology for 304 Stainless Steel Thick Plates and the Mechanical Properties of Welding Joints,” *Coatings*, vol. 12, no. 1, Jan. 2022, doi: 10.3390/coatings12010059.

[21] A. Klimpel, A. Lisiecki, A. Klimpel, and A. Lisiecki, “Laser welding of butt joints of austenitic stainless steel AISI 321 Laser welding of butt joints of austenitic stainless steel AISI 321 Manufacturing and processing,” 2007. [Online]. Available: https://www.researchgate.net/publication/40624473

[22] F. Kong, W. Liu, J. Ma, E. Levert, and R. Kovacevic, “Feasibility study of laser welding assisted by filler wire for narrow-gap butt-jointed plates of high-strength steel,” *Welding in the World*, vol. 57, no. 5, pp. 693–699, Sep. 2013, doi: 10.1007/s40194-013-0068-9.

[23] K. Mao, H. Wang, Y. Wu, V. Tomar, and J. P. Wharry, “Microstructure-property relationship for AISI 304/308L stainless steel laser weldment,” *Materials Science and Engineering: A*, vol. 721, pp. 234–243, Apr. 2018, doi: 10.1016/J.MSEA.2018.02.092.

[24] Z. Wang, T. A. Palmer, and A. M. Beese, “Effect of processing parameters on microstructure and tensile properties of austenitic stainless steel 304L made by directed energy deposition additive manufacturing,” *Acta Materialia*, vol. 110, pp. 226–235, May 2016, doi: 10.1016/j.actamat.2016.03.019.

[25] R. K. Desu, H. Nitin Krishnamurthy, A. Balu, A. K. Gupta, and S. K. Singh, “Mechanical properties of Austenitic Stainless Steel 304L and 316L at elevated temperatures,” *Journal of Materials Research and Technology*, vol. 5, no. 1, pp. 13–20, Jan. 2016, doi: 10.1016/j.jmrt.2015.04.001.

[26] M. S. Loveday, T. Gray, and J. Aegerter, “Tensile Testing of Metallic Materials: A Review.” [Online]. Available: http://www.npl.co.uk/npl/cmmt/projects/tenstand/

[27] A. E. Matusevich, J. C. Massa, and R. A. Mancini, “Computation of tensile strain-hardening exponents through the power-law relationship,” *Journal of Testing and Evaluation*, vol. 40, no. 4, Jul. 2012, doi: 10.1520/JTE104226.

[28] J. S. Weaver *et al.*, “Spherical nanoindentation of proton irradiated 304 stainless steel: A comparison of small scale mechanical test techniques for measuring irradiation hardening,” *Journal of Nuclear Materials*, vol. 493, pp. 368–379, Sep. 2017, doi: 10.1016/j.jnucmat.2017.06.031.

[29] M. Natali, G. Carta, V. Rigato, G. Rossetto, G. Salmaso, and P. Zanella, “Chemical, morphological and nano-mechanical characterizations of Al 2O3 thin films deposited by metal organic chemical vapour deposition on AISI 304 stainless steel,” *Electrochimica Acta*, vol. 50, no. 23 SPEC. ISS., pp. 4615–4620, Aug. 2005, doi: 10.1016/j.electacta.2004.10.097.

[30] K. Y. Luo *et al.*, “Effects of laser shock processing on mechanical properties and micro-structure of ANSI 304 austenitic stainless steel,” *Materials Science and Engineering A*, vol. 528, no. 13–14, pp. 4783–4788, May 2011, doi: 10.1016/j.msea.2011.03.041.

[31] Y. Lu *et al.*, “Conversion between Vickers hardness and nanohardness by correcting projected area with sink-in and pile-up effects,” *Plasma Science and Technology*, vol. 22, no. 6, 2020, doi: 10.1088/2058-6272/ab7d47.

[32] C. Y. Cui, X. G. Cui, X. D. Ren, T. T. Liu, J. D. Hu, and Y. M. Wang, “Microstructure and microhardness of fiber laser butt welded joint of stainless steel plates,” *Materials and Design*, vol. 49, pp. 761–765, 2013, doi: 10.1016/j.matdes.2013.02.059.

[33] H. Fujita and T. Katayama, “In-situ observation of strain-induced γ→ε→α′ and γ→α′ martensitic transformations in Fe–Cr–Ni alloys,” *Materials Transactions, JIM*, vol. 33, no. 3, 1992, doi: 10.2320/matertrans1989.33.243.

[34] William D. Callister Jr. and David G. Rethwisch, *Materials Science and Engineering: An Introduction*. Hachette Livre - Département Pratique, 2018.

[35] M. J. Swenson, C. K. Dolph, and J. P. Wharry, “The effects of oxide evolution on mechanical properties in proton- and neutron-irradiated Fe-9%Cr ODS steel,” *Journal of Nuclear Materials*, vol. 479, pp. 426–435, Oct. 2016, doi: 10.1016/J.JNUCMAT.2016.07.022.

[36] C. R. Barrett, W. D. Nix, and A. S. Tetelman, “The Principles of Engineering Materials,” p. 554, 1973, Accessed: Mar. 20, 2022. [Online]. Available: https://books.google.com/books/about/The_Principles_of_Engineering_Materials.html?id=-ZxRAAAAMAAJ

[37] Q. Xue, M. A. Meyers, and V. F. Nesterenko, “Self organization of shear bands in stainless steel,” *Materials Science and Engineering: A*, vol. 384, no. 1–2, pp. 35–46, Oct. 2004, doi: 10.1016/J.MSEA.2004.05.069.

[38] R. G. (Richard G. Budynas, J. Keith. Nisbett, and J. Edward. Shigley, “Shigley’s mechanical engineering design,” p. 1059, 2008.

[39] M. Mata, O. Casals, and J. Alcalá, “The plastic zone size in indentation experiments: The analogy with the expansion of a spherical cavity,” *International Journal of Solids and Structures*, vol. 43, no. 20, pp. 5994–6013, Oct. 2006, doi: 10.1016/j.ijsolstr.2005.07.002.

# Appendix A: X-ray diffraction data manipulation

The following outlines the process that was used to manipulate the XRD data. This example uses data from a test run of the XRD performed on the weld material of the tensile tested sample. Figure A.1 shows the original, unmanipulated data split into two “Steps”, these represent each scan step described in chapter 2.

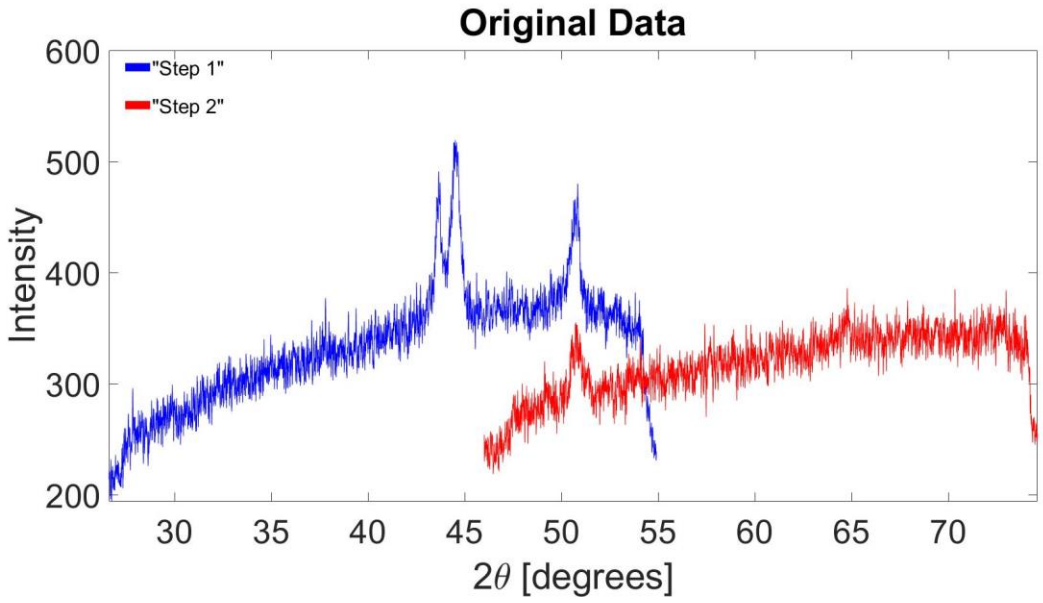


Figure A.1 Original XRD data.

Next, each step was fit with a first-degree polynomial. Figure A.2 shows the original data with each trendline.

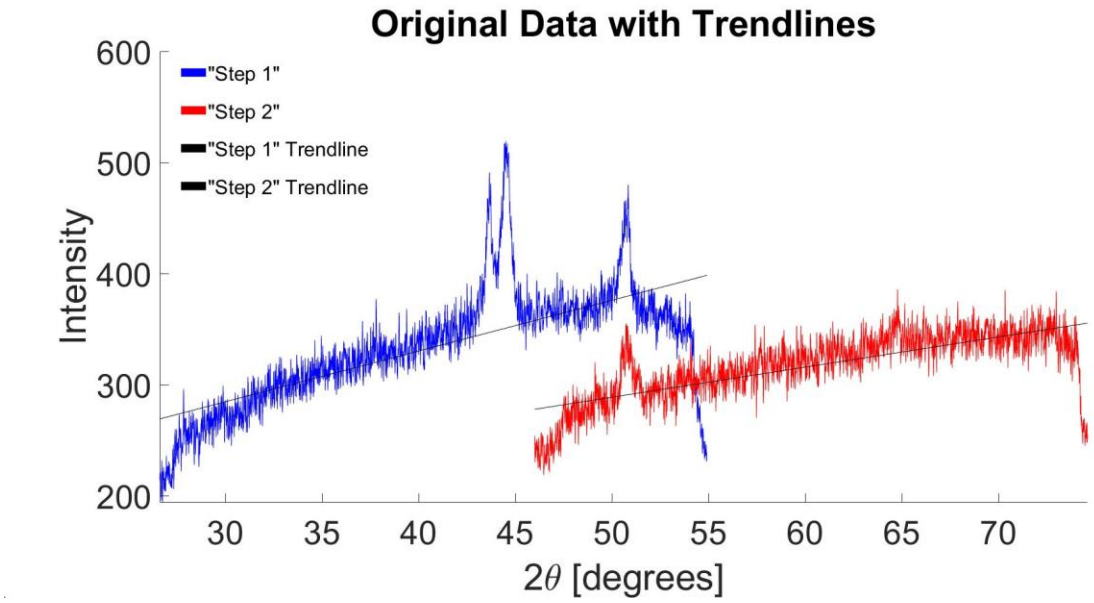


Figure A.2 Original data with trendlines.

These trendlines were then subtracted from each scan data to achieve an average of 0 intensity. The result of this is shown in Figure A.3.

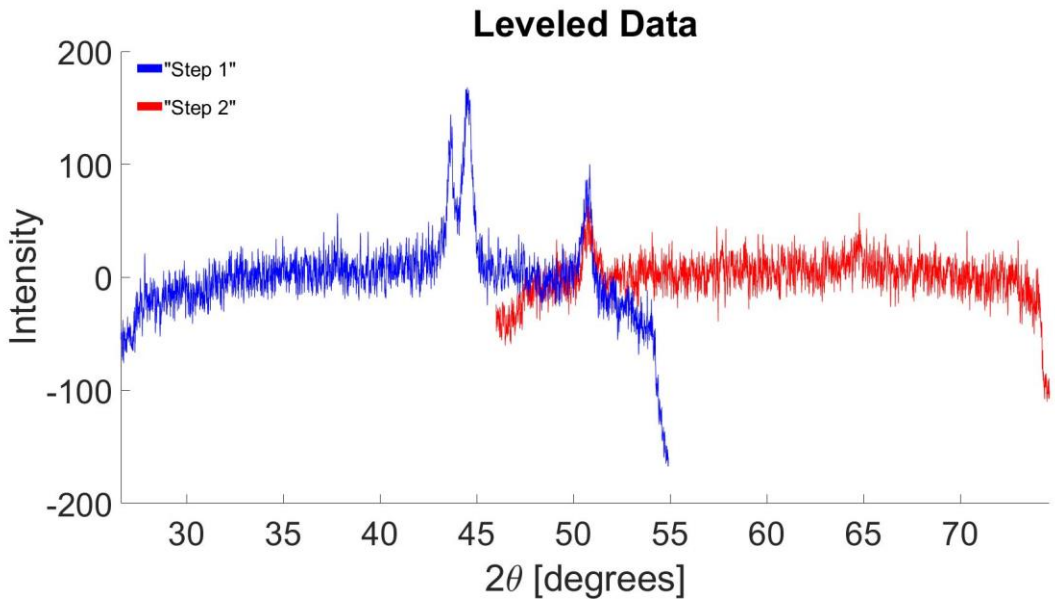


Figure A.3 Leveled data.

Finally, a point was chosen that each scan overlapped. The data of each scan was then truncated to this point. This is shown in Figure A.4.

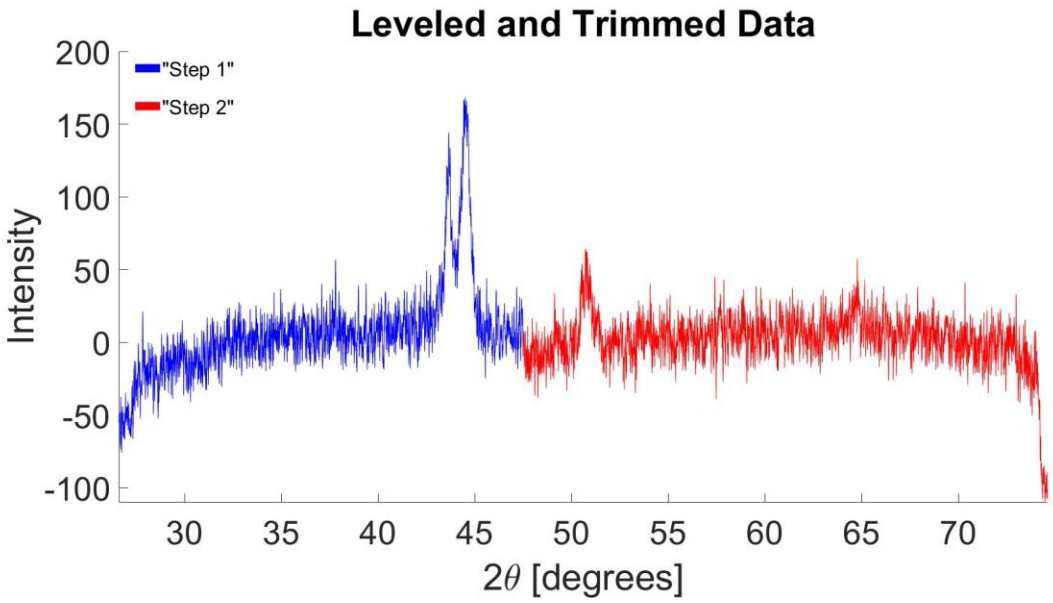


Figure A.4 Leveled and trimmed data.